nature genetics

Article

https://doi.org/10.1038/s41588-025-02188-0

Three-dimensional genome landscape of primary human cancers

Received: 29 November 2023

Accepted: 2 April 2025

Published online: 12 May 2025

Check for updates

Kathryn E. Yost[1,2,31,32], Yanding Zhao[1,2,3,32], King L. Hung[1,2], Kaiyuan Zhu[4], Duo Xu[5,6,30], M. Ryan Corces[7,8,9], Shadi Shams[1,2], Bryan H. Louie[1,2], Shahab Sarmashghi[10], Laksshman Sundaram[3,11,12,13], Jens Luebeck[4], Stanley Clarke[14,15,16,17], Ashley S. Doane[18], Jeffrey M. Granja[1,2,3], Hani Choudhry[19], Marcin Imieliński[15,16,17], Andrew D. Cherniack[10,20,21], Ekta Khurana[5,6,22,23], Vineet Bafna[4], Ina Felau[24], Jean C. Zenklusen[24], Peter W. Laird[25], Christina Curtis[3,26,27], Cancer Genome Atlas Analysis Network*, William J. Greenleaf[3,28] ✉ & Howard Y. Chang[1,2,29] ✉

Genome conformation underlies transcriptional regulation by distal enhancers, and genomic rearrangements in cancer can alter critical regulatory interactions. Here we profiled the three-dimensional genome architecture and enhancer connectome of 69 tumor samples spanning 15 primary human cancer types from The Cancer Genome Atlas. We discovered the following three archetypes of enhancer usage for over 100 oncogenes across human cancers: static, selective gain or dynamic rewiring. Integrative analyses revealed the enhancer landscape of noncancer cells in the tumor microenvironment for genes related to immune escape. Deep whole-genome sequencing and enhancer connectome mapping provided accurate detection and validation of diverse structural variants across cancer genomes and revealed distinct enhancer rewiring consequences from noncoding point mutations, genomic inversions, translocations and focal amplifications. Extrachromosomal DNA promoted more extensive enhancer rewiring among several types of focal amplification mechanisms. These results suggest a systematic approach to understanding genome topology in cancer etiology and therapy.

In every human cell, 2 m of DNA is extensively folded within a ~10-µm nucleus. Eukaryotic genomes are hierarchically organized in three dimensions to enable transcriptional regulation by distal *cis*-regulatory elements. Chromosomes are subdivided into multimegabase (Mb) A and B compartments, which interact in a homotypic fashion and are enriched for euchromatin versus heterochromatin, respectively[1]. Megabase-sized topologically associating domains (TADs) facilitate DNA interactions within TADs but generally exclude interactions between TADs[2–6]. Enhancer–promoter (E–P) loops connect distal enhancers to target genes located 10–100 kilobases away, enabling cell-type-specific gene expression[7–9]. These three scales of genome architecture can operate independently[10]. Alterations in gene expression, DNA methylation and chromatin accessibility are widespread in primary human cancers[11,12]. However, functionally linking *cis*-regulatory elements to target genes remains challenging due to regulatory element redundancy, cell-type-specific activity and large genomic distances between *cis*-regulatory elements and their target genes[13]. While prior studies have illustrated the potential impact of altered chromosome topology on enhancer rewiring in cancer[14], a systematic understanding of the three-dimensional (3D) architecture of cancer genomes is

A full list of affiliations appears at the end of the paper. ✉e-mail: wjg@stanford.edu; howchang@stanford.edu

still lacking. Differences in 3D genome organization between cell line models and primary tissue[15] as well as patient-specific genetic alterations highlight the importance of chromosome conformation profiling in primary cancer samples.

Cancer genomes are characterized by frequent structural variations (SVs) that have the potential to alter 3D genome organization, enabling interactions with otherwise distant regulatory elements[16,17]. In addition to simple SVs, including duplications, deletions, inversions and translocations[17], ongoing genomic instability in cancer can lead to complex structures through chromothripsis, breakage-bridge fusion events and extrachromosomal DNA (ecDNA) formation. ecDNAs are ~100-kb- to 5-Mb-sized circular DNA molecules that enable massive oncogene expression and lead to poor patient outcome[18]. SVs can lead to alterations in both gene copy number (CN) and DNA element connectivity, but the functional consequences on gene regulation are poorly understood[19,20]. Chromosome conformation has emerged as a powerful tool to assemble and characterize SVs[21]. Mapping the 3D cancer genome may clarify the structure of SVs as well as determine their functional consequences on gene regulation.

Here we map the enhancer connectome of primary human cancers by HiChIP, a protein-directed chromosome conformation method, to simultaneously assess enhancer activity measured by histone H3 lysine 27 acetylation (H3K27ac) and interactions with target loci[22,23], two features that are jointly predictive of gene expression[24]. We leverage and integrate multidimensional data from The Cancer Genome Atlas (TCGA), including expanded deep whole-genome sequencing (WGS) and single-cell chromatin accessibility mapping with 3D genome architecture, to address the role of chromosome topology in cancer gene regulation.

Results

Multiple scales of 3D genome organization in human cancers

We profiled genome-wide chromosome conformation in 69 tumor samples representing 15 primary human cancer types using H3K27ac HiChIP[22,23] (Methods). These 15 cancer types were chosen based on overlap with samples previously profiled by the assay of transposase-accessible chromatin using sequencing (ATAC–seq)[12] and to represent the diversity of human cancers (Fig. 1a and Supplementary Table 1). All HiChIP experiments demonstrated signal enrichment at gene promoters and sufficient numbers of uniquely mapped contacts for further analysis (Extended Data Fig. 1a–c). To enable integration with additional donor-matched data generated by TCGA, including ATAC–seq, RNA sequencing (RNA-seq) and WGS data, we validated donor identity based on single-nucleotide polymorphism (SNP) genotyping calls (Extended Data Fig. 1d)[12]. WGS of 268 TCGA samples analyzed for chromatin accessibility was also extended to 75× coverage for tumor samples and 25× coverage for matched normal samples to facilitate interpretation of CN variations (CNVs), point mutations and SVs (Extended Data Fig. 1e,f and Supplementary Table 2; Methods).

We identified 665,682 unique significant interactions, or loops, associated with putative regulatory elements marked by H3K27ac, including complex E–P interactions such as enhancer-skipping of nearest genes (Fig. 1b and Extended Data Fig. 2a–f). Additionally, we compared our pan-cancer loop set with previously identified loops from H3K27ac HiChIP profiling of cell lines and primary tissue samples (Extended Data Fig. 2g)[25]. Overall, 71% of our loops overlapped with previously identified loops, and we also identified 188,887 looping interactions not observed in previous datasets. HiChIP interaction matrices revealed A/B compartment level organization at the megabase scale reflected in the first eigenvector of the correlation matrix, which was largely consistent across different cancer types and concordant with A/B compartments estimated from DNA methylation correlation matrices[26] (Fig. 1c,d and Extended Data Fig. 2h).

To explore enhancer connectome diversity between different cancer types, we first considered the *MYC* oncogene located on chromosome 8, which is regulated by surrounding tissue-specific enhancers[12,27]. We assessed one-dimensional (1D) H3K27ac ChIP enrichment detected by HiChIP and observed H3K27ac enrichment either at regulatory elements located 5′ of *MYC* in cancer types such as colon adenocarcinoma (COAD) or at 3′ regulatory elements as in liver hepatocellular carcinoma (LIHC; Fig. 1d,e). This bias in H3K27ac reflected tissue-specific H3K27ac enrichment observed in healthy colon and liver, as well as previously observed trends in chromatin accessibility from matched samples[12,28] (Fig. 1e and Extended Data Fig. 2i). Furthermore, we observed corresponding biases in 3D organization at the *MYC* locus using HiChIP, reflected in differential contact frequency in the interaction matrix and direction of significant loops linked to the *MYC* promoter (Fig. 1e and Extended Data Fig. 2j). Finally, 5′ or 3′ bias in enhancer activity was also reflected in enhancer interaction signal (EIS) at the *MYC* promoter, as determined by virtual 4C analysis, which reflects both H3K27ac ChIP signal strength and chromosome conformation contact strength with the designated anchor (Fig. 1d,e).

We further examined the scales of genome topology that distinguished human cancer types, leveraging the multiscale data yielded by HiChIP. We noted that H3K27ac enrichment as well as 2D interaction signals were impacted by CNVs, and for subsequent analyses, we applied CN correction based on WGS ploidy-corrected CNV calls, excluding seven samples without matched WGS from further analysis (Extended Data Fig. 2k; Methods). First, we performed Pearson correlation and hierarchical clustering using vectorized subcompartment annotations reflecting higher order chromosome conformation[29] (Fig. 1f). Individual samples exhibited high pairwise correlation at the subcompartment level, and some cancer types were not well separated by hierarchical clustering, similar to prior observations of conserved compartment organization between different cell and tissue types[1,8,30]. Second, we found that 1D H3K27ac enrichment associated with cell-type-specific enhancers[31,32] provided better cancer-type specificity, reflected in a higher cluster purity and lower cluster entropy following hierarchical clustering (Fig. 1f and Extended Data Fig. 2l; Methods). Finally, 2D HiChIP signal at significant interactions in the union loop set provided the best separation between different cancer types, and clustering was concordant with prior clustering based on bulk RNA-seq, ATAC–seq and DNA methylation[12] (Fig. 1f and Extended Data Fig. 3a).

Dimensionality reduction of either H3K27ac peak or HiChIP loop signal, followed by *t*-distributed stochastic neighbor embedding, also separated samples by cancer type and was consistent with previously described ATAC–seq clusters (Extended Data Fig. 3b–d)[12]. Additionally, sample clustering reflected additional features, such as separation between basal and nonbasal breast cancers (Extended Data Fig. 3e) and differences between esophageal squamous cell carcinoma (ESCC) and esophageal adenocarcinoma (EAC; Extended Data Fig. 3f)[33]. To identify differential H3K27ac peaks and HiChIP loops, we used feature binarization[12,34] to identify features that are unique to a specific cancer type or subset of cancer types and identified 28,716 differential H3K27ac peaks and 5,073 differential loops (Extended Data Fig. 4a,b). Consistent with prior results from chromatin accessibility profiling, cancer-type-specific peaks and loops identified by HiChIP were enriched for relevant transcription factor (TF) motifs, including p63 in squamous cancers (ESCC and lung squamous cell carcinoma (LUSC)) and androgen response elements in prostate adenocarcinomas (PRAD; Extended Data Fig. 4c,d). Interestingly, we noted that some TFs were preferentially enriched in H3K27ac-associated loops relative to H3K27ac peaks, suggesting that these TFs may potentially be more relevant for 3D looping interactions. Expanding on our observation of cancer-type-specific regulation of *MYC*, we identified 51 oncogenes with >5 linked differential H3K27ac peaks, nominating tissue-specific regulatory elements (Extended Data Fig. 4e and Supplementary Table 3).

Furthermore, we noted multiple loci that were enriched for H3K27ac in multiple cancer types but engaged in differential looping

https://doi.org/10.1038/s41588-025-02188-0

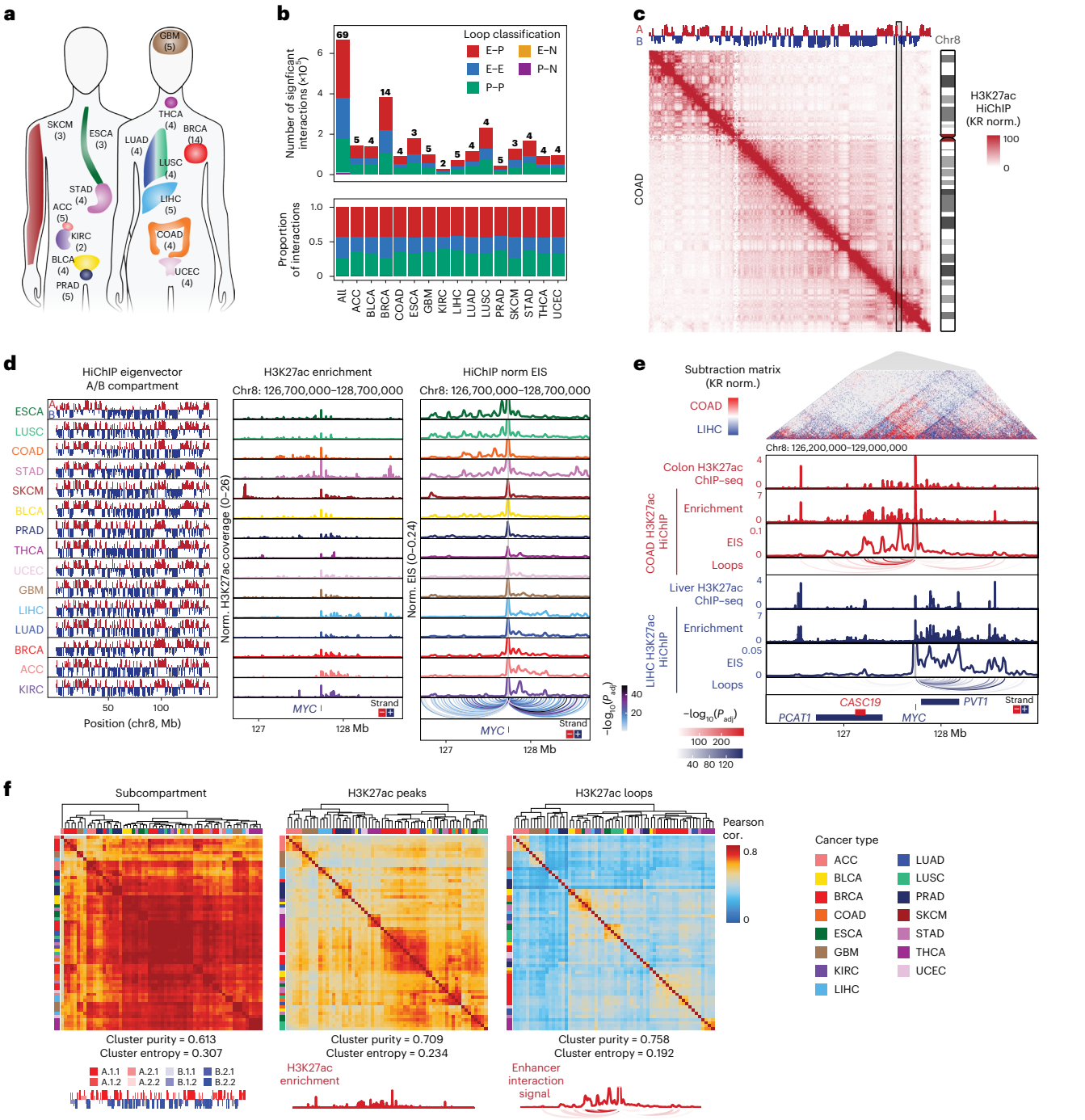

Fig. 1 | HiChIP identifies high-resolution chromosome conformation in primary human cancers across multiple scales. a, Schematic representation of the 15 cancer types profiled in this study. **b**, Stacked bar plot of the number of unique significant FitHiChIP interactions identified by H3K27ac HiChIP by cancer type and colored by loop classification (E–P, E–E, P–P, E–N and P–N). The numbers shown above each bar represent the number of samples profiled for each cancer type. **c**, KR matrix balancing-normalized H3K27ac HiChIP contact matrix at 250-kb resolution for merged COAD samples on chromosome 8. Top track displays the first principal component of Pearson's matrix eigenvector of the KR-normalized observed/expected matrix, corresponding to A/B compartment. **d**, First eigenvector of the KR-normalized observed/expected matrix, corresponding to A/B compartment, for all samples merged by cancer type (left). One-dimensional H3K27ac signal enrichment at the *MYC* locus normalized by reads overlapping TSS for all samples merged by cancer type (middle). Interaction profiles of the *MYC* promoter representing EIS for all samples merged by cancer type (right). Significant loop interactions colored by adjusted *P* value are shown below. *P* values were calculated using a two-sided binomial test and corrected using the BH procedure. Cancer types are ordered based on H3K27ac signal bias at the *MYC* locus. **e**, Subtraction matrix comparing KR-normalized H3K27ac HiChIP at 10-kb resolution from merged COAD and LIHC samples at the *MYC* locus (top). Tracks visualize H3K27ac ChIP–seq enrichment from normal tissue profiled by ENCODE, HiChIP 1D H3K27ac enrichment, interaction profiles of the *MYC* promoter, and significant loop interactions colored by adjusted *P* value. *P* values were calculated using a two-sided binomial test and corrected using the BH procedure. **f**, Unsupervised hierarchical clustering of vectorized HiChIP subcompartment annotations (left), HiChIP 1D H3K27ac signal (middle), and HiChIP 2D interaction signal (right). Heatmap colored by Pearson correlation coefficients. Cluster purity quantifies the degree that samples of the same cancer type cluster together with higher values, indicating better clustering performance, while for cluster entropy, lower values indicate better clustering performance. Representative subcompartments, H3K27ac enrichment and EIS tracks illustrating the data type used for correlation analysis are shown at bottom.

https://doi.org/10.1038/s41588-025-02188-0

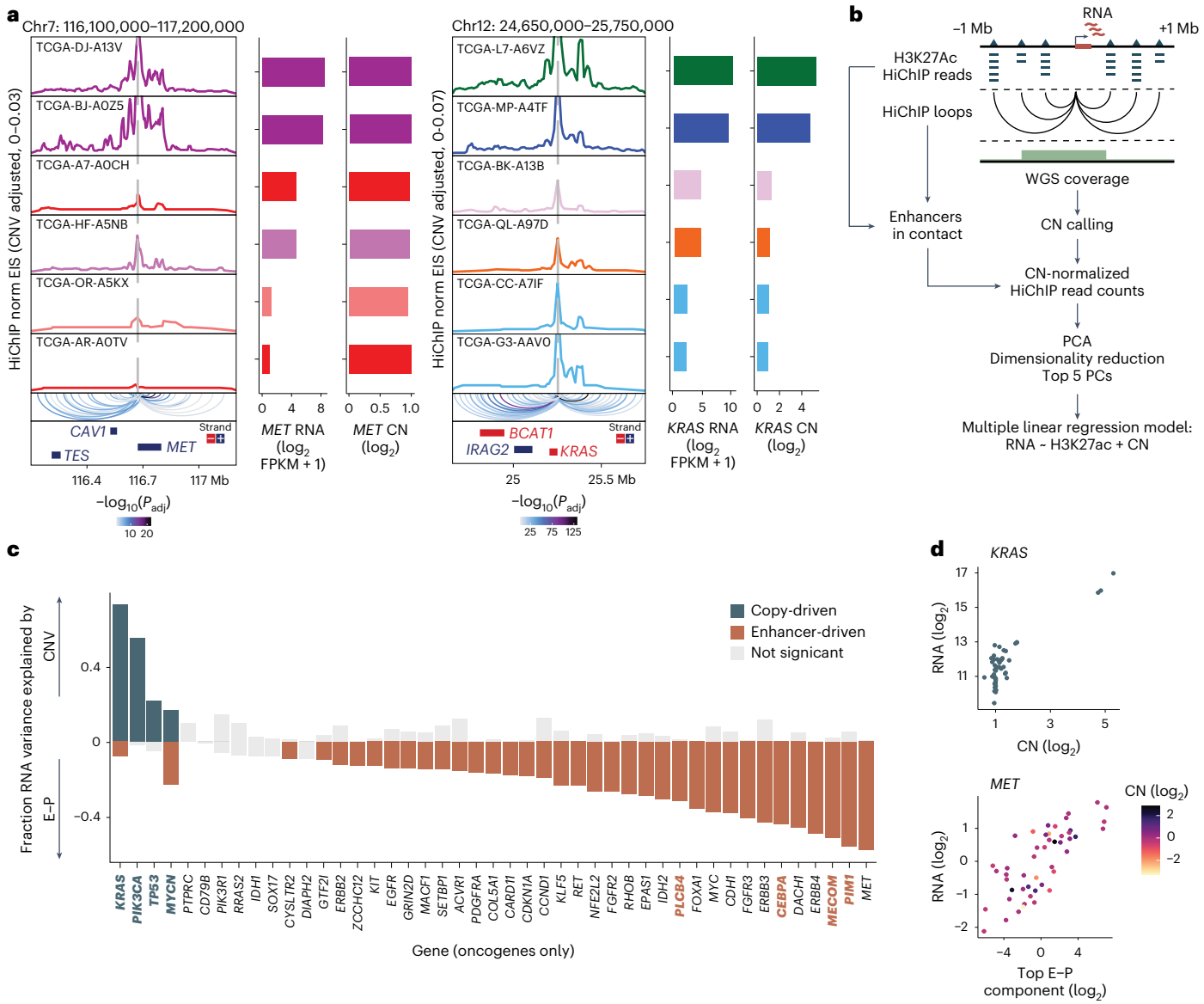

Fig. 2 | Differential contributions of CN and enhancer activity explain variability in oncogene expression. a, Interaction profiles of the *MET* and *KRAS* promoters for individual samples with high (rank 1 and 2 of 56 samples with matched RNA-seq, WGS and HiChIP data), intermediate (rank 28 and 29) or low (rank 55 and 56) RNA expression with significant loop interactions colored by adjusted *P* value. *P* values were calculated using a two-sided binomial test and corrected using the BH procedure. Bar plots visualize RNA expression and CN inferred from WGS. **b**, Schematic representation of analysis to infer contribution of enhancer interaction gain or gene CN to oncogene mRNA expression level. **c**, Oncogenes with variance in RNA expression >1 ($n = 45$) ranked by the fraction of RNA variance explained by CNV or linked enhancer activity across cancer samples. Each column is a gene. Genes with dark blue-colored bars on the top are significantly explained by CNV, while genes with orange-colored bars on the bottom are significantly explained by enhancer signal (E–P; H3K27ac term with the highest relative importance for each gene is shown). Genes in bold dark blue or orange text are also significant when cancer type is included in regression analysis. **d**, Scatter plot of the relationship between DNA CN and RNA expression for copy-driven gene *KRAS* (top) and E–P interaction signal and RNA expression for enhancer-driven gene *MET* (bottom). FPKM, fragments per kilobase of transcript per million mapped reads.

in specific cancer types, although most differential peaks overlapped with a differential loop (Extended Data Fig. 4f). For example, we identified a putative regulatory element located −9 kb of the *ESR1* gene encoding estrogen receptor α that is marked by H3K27ac in nonbasal breast invasive carcinomas (BRCA), thyroid carcinoma (THCA) and uterine corpus endometrial carcinoma (UCEC), but with increased looping to the *ESR1* promoter in UCEC, which correlates with higher *ESR1* expression (Extended Data Fig. 4g). Additionally, we identified more complex examples, such as an H3K27ac peak overlapping histone H4 gene *H4-16* with differential looping interactions to several nearby genes that correlates with the expression of the interacting gene (Extended Data Fig. 4h). These results suggest that 3D cancer genomes have globally similar compartment organization, but enhancer-associated histone modifications and fine-scale E–P loops distinguish different cancer types.

Oncogene expression by enhancer rewiring or CN gain

We next examined the roles of the 3D genome in oncogene transcription. We focused on 110 consensus driver oncogenes that were found to be recurrently mutated or overexpressed across different cancer types[35]. The 3D chromatin landscape across cancer types suggested the following three classifications of enhancer usage: (1) static enhancer usage, exemplified by *NRAS* (encoding neuroblastoma RAS viral oncogene homolog); (2) selective enhancer connectivity in one cancer

https://doi.org/10.1038/s41588-025-02188-0

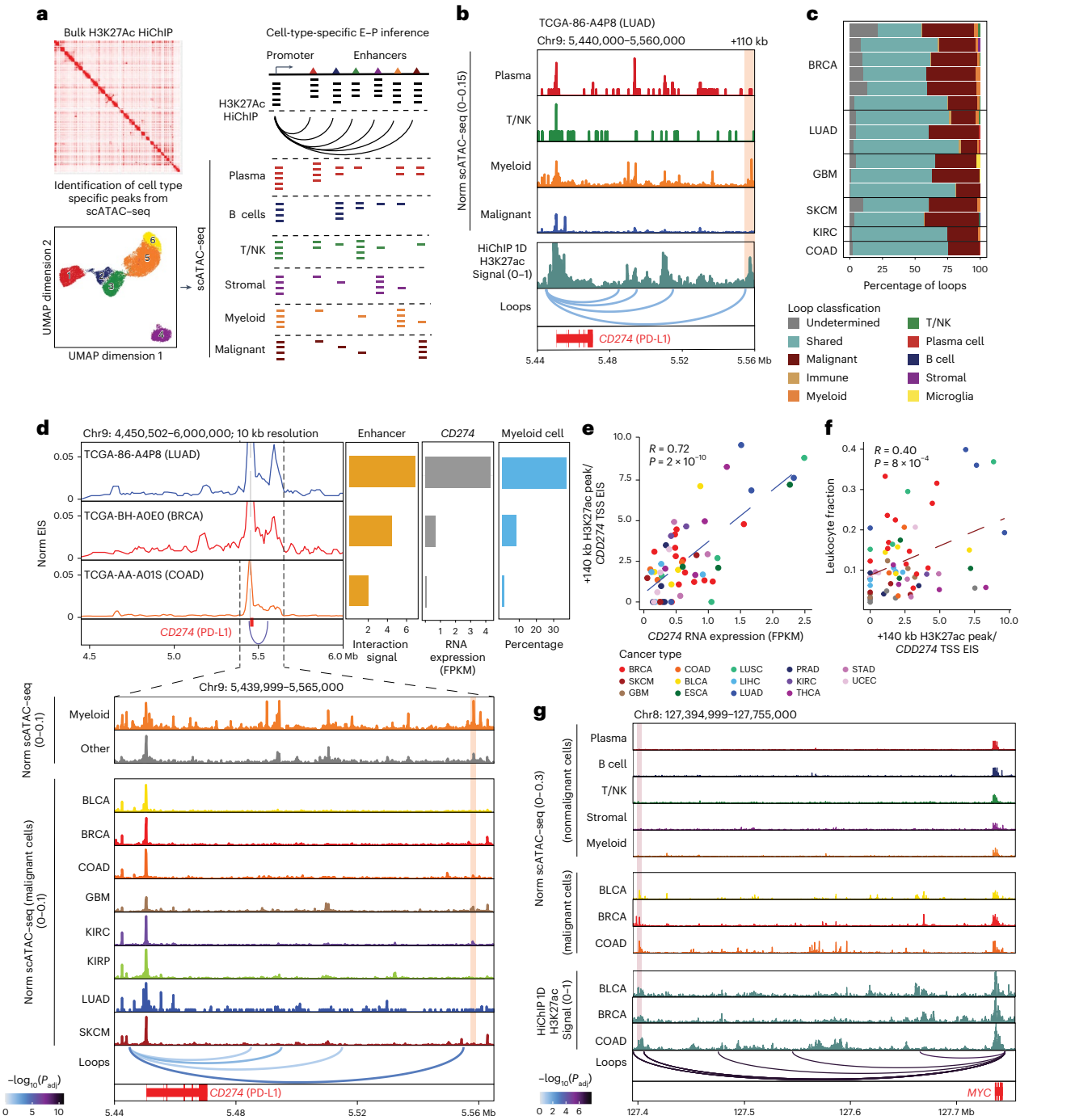

Fig. 3 | Deconvolution of HiChIP signal resolves malignant and immune cell-specific chromatin conformation in TME. a, Schematic representation showing identification of cell-type-specific enhancer–promoter interactions using integration of HiChIP and scATAC–seq data. **b**, Signal tracks showing scATAC–seq and H3K27ac HiChIP at *CD274* locus (encoding PD-L1) for sample TCGA-86-A4P8. The scATAC–seq track indicates the chromatin accessibility of different cells in TME (top). The H3K27ac HiChIP track indicates the bulk H3K27ac signal (middle). The interaction track indicates the *CD274* promoter-associated interactions. The shaded area indicates the myeloid cell-specific H3K27ac peak. **c**, Bar plot of loop annotation based on scATAC–seq/HiChIP integration for samples with matched scATAC and H3K27ac HiChIP. **d**, Integrative virtual 4C and scATAC–seq signal tracks showing the myeloid cell-specific enhancer–promoter interaction for *CD274* (encoding PD-L1). The virtual 4C plot shows the EIS changes (left) with matched *CD274* RNA expression and myeloid cell percentages based on scATAC–seq (right). The scATAC–seq track indicates the chromatin accessibility of myeloid cells, noncancer cells and cancer cells across eight different cancer types (bottom). The marked area indicated the myeloid cell-specific H3K27ac peak. Significant loop interactions are colored by adjusted *P* value, and *P* values were calculated using a two-sided binomial test and corrected using the BH procedure. **e**, Scatter plot showing the correlation between the enhancer–promoter interaction and *CD274* RNA expression. The correlation coefficient was calculated using Pearson correlation, and the *P* value was calculated using a two-sided *t* test. **f**, Scatter plot showing the correlation between the enhancer–promoter interaction and RNA-seq-derived leukocyte fraction estimation. The correlation coefficient was calculated using Pearson correlation, and the *P* value was calculated using a two-sided *t* test. **g**, Signal tracks showing the integrative track of scATAC–seq and H3K27ac HiChIP at *MYC* locus. The scATAC–seq track indicates the chromatin accessibility of different noncancer and cancer cells in eight cancer types (top). The H3K27ac HiChIP track indicates the bulk level H3K27ac signal in BLCA, BRCA and COAD (middle). The interaction track indicates the *MYC* promoter-associated interactions. The shaded area indicates H3K27ac peaks that overlap with cancer risk-associated SNPs. Significant loop interactions are colored by adjusted *P* value, and *P* values were calculated using a two-sided binomial test and corrected using the BH procedure.

type, such as *EGFR* (encoding epidermal growth factor receptor) in glioblastoma; and (3) highly dynamic patterns of enhancer contacts, including *MYC* (encoding MYC proto-oncogene, bHLH transcription factor; Fig. 1d, Extended Data Fig. 5a,b and Supplementary Table 4). Individual oncogenes varied considerably in the number of E–P loops identified by HiChIP, suggesting that enhancer activity may contribute to RNA expression in a gene-specific manner (Extended Data Fig. 5c).

In addition to enhancer rewiring, DNA CN has a profound effect on oncogene expression. Not only do amplified genes tend to be more highly expressed due to additional DNA copies, but they may also explore different gene regulatory space[19,20,36]. We first compared CN and enhancer activity for cases with low, intermediate or high RNA expression and found variable contributions depending on the gene. For example, *MET* showed a strong correlation between H3K27ac HiChIP signal and RNA expression with minimal changes in DNA CN (Fig. 2a). In contrast, differences in *KRAS* RNA expression reflected DNA CNVs while H3K27ac HiChIP signal was largely unchanged. To determine the relative contributions of both enhancer usage and CNVs on oncogene transcription, we performed an integrated analysis using H3K27ac HiChIP, bulk RNA-seq and WGS. We used multiple linear regression to determine the relative contributions of DNA CN and enhancer interaction score to variance in RNA expression across all driver oncogenes and cancer types (Fig. 2b). To account for multiple coordinated enhancers, for each gene, we identified all significant HiChIP looping interactions as well as overlapping H3K27ac peaks and took the top five principal components of H3K27ac signal across all samples (Extended Data Fig. 5d). We noted correlations between DNA CN and the first principal component of H3K27ac signal, which was mitigated by CN regression (Extended Data Fig. 5e).

Overall, we found that both H3K27ac signal and DNA CN explained variance in RNA expression, although individual genes differed substantially in how much variance in RNA expression could be explained by either CN or enhancer activity (Fig. 2c and Extended Data Fig. 5f,g). Given the prevalence of cancer-type-specific enhancers, we also performed regression analysis with cancer type included and found that while cancer type explains a considerable proportion of variance and reduces the variance explained by E–P signal, the variance explained per gene for both CN and E–P signal is highly correlated in both analyses (Extended Data Fig. 5f,h,i). Quantitative analysis showed that for the majority of all genes and over 70% of oncogenes, mRNA expression is better explained by gains in enhancer activity, while expression of the remaining genes is better explained by DNA CN (Fig. 2c and Extended Data Fig. 6a). When comparing to patterns of static, selective or dynamic enhancer usage as defined above, we find that only oncogenes with selective and static enhancer usage were copy-driven, while all classes of enhancer usage can be enhancer-driven (Extended Data Fig. 6a). While some of the top copy-driven oncogenes have more extreme variation in CN, several enhancer-driven oncogenes have comparable variation in CN, suggesting that gene classification is not solely driven by extreme changes in CN (Extended Data Fig. 6b). The pattern of enhancer or copy-driven oncogene expression is remarkably binary and consistent (Fig. 2d and Extended Data Fig. 6c,d). This analysis demonstrates that CN amplification explains overexpression for a few oncogenes, while enhancer activity better accounts for most cases, highlighting the role of the 3D regulatory landscape in oncogene activation.

Cell-type-specific E–P loops in the tumor microenvironment (TME)

Epigenetic regulation of immune cells profoundly impacts cancer development; however, knowledge regarding enhancer–promoter interactions in the TME is limited. We developed a computational framework to deconvolute H3K27ac HiChIP into cell-type-specific signals using patient-matched single-cell ATAC–seq (scATAC–seq)[37] (Fig. 3a and Supplementary Table 5; Methods). For instance, we identified a myeloid cell-specific enhancer–promoter interaction for the *CD274* gene (encoding programmed death-ligand 1 (PD-L1)) in lung adenocarcinoma (LUAD) sample TCGA-86-A4P8 (Fig. 3b). HiChIP revealed an interaction between the *CD274* promoter and a regulatory element marked by H3K27ac located +110 kb away, adjacent to previously described enhancers[38]. scATAC–seq analysis from the same sample validated myeloid-specific accessibility at this enhancer, with minimal accessibility in malignant or other immune cells. In contrast, an enhancer −140 kb away from the promoter of the *CCND3* gene (cyclin D3) displayed chromatin accessibility specific to malignant cells (Extended Data Fig. 7a).

We extended this framework to 29 patients with matched H3K27ac HiChIP and scATAC–seq, focusing on 16 samples with sufficient nonmalignant cells for scATAC–seq peak calling (Methods). Most E–P interactions overlapped with scATAC–seq peaks that were accessible across multiple cell types; however, we were able to identify cell-type-specific interactions (Fig. 3c). In total, we identified 1,551 malignant cell-specific and 745 immune cell-specific interactions. Immune cell-associated E–P interactions displayed significantly lower correlation with tumor purity and higher correlation with RNA-seq-derived leukocyte fraction estimates compared to malignant cell-associated E–P interactions (Extended Data Fig. 7b,c; Methods)[39,40]. Gene Ontology analysis revealed that malignant cell enhancer contacts were enriched for cell division and growth genes, while those in tumor-associated myeloid, B and T/natural killer (NK) cells were linked to immune pathways (Extended Data Fig. 7d).

PD-L1, encoded by *CD274*, is a 'don't kill me' signal that dampens anticancer T cell responses and is a major target for cancer immunotherapy[41]. While commonly expressed by malignant cells, PD-L1 is also highly expressed by immune cells in the TME, including macrophages and dendritic cells[42]. We identified a dynamic enhancer located 110 kb 3′ of *CD274* with E–P interaction signal correlated with *CD274* mRNA expression, leukocyte fraction estimation and myeloid cell frequency estimated by scATAC–seq (Fig. 3d–f, Extended Data Fig. 7e and Supplementary Table 6; Methods). Pseudobulk single-cell chromatin accessibility analysis further supported the myeloid specificity of this enhancer, which was uniquely accessible in myeloid cells (Fig. 3d). We also examined T/NK cell-specific E–P interactions for *IKZF1*, a known regulator of immune cell development expressed by multiple immune cell types, including T cells[43]. While the *IKZF1* promoter is accessible across multiple immune cell types in the TME, we identified an intronic, T/NK cell-specific enhancer with significant looping to the promoter (Extended Data Fig. 7f). The *IKZF1* E–P interaction signal correlated positively with *IKZF1* RNA expression as well as leukocyte fraction estimation but negatively with tumor purity estimation (Extended Data Fig. 7g,h). In addition, many E–P interactions exhibited shared chromatin accessibility between malignant and immune cells, including immune checkpoint genes like *CTLA4*, *TIGIT*, *VSIR* and *TIM3* (refs. 44,45; Supplementary Table 6 and Extended Data Fig. 7i). These results suggest that the immunological setpoints of cancers reflect the contributions of multiple cell types in the TME.

scATAC–seq-based deconvolution enabled the classification of malignant cell-specific E–P interactions, nominating enhancers linked to altered gene expression in transformed cells (Fig. 3c). Gene Ontology analysis revealed that one of the most significantly enriched sets of enhancer target genes is the MYC pathway (Extended Data Fig. 7d). We enumerated malignant cell-specific E–P loops at the *MYC* locus in BLCA, BRCA and COAD samples (Fig. 3g). *MYC* EIS positively correlated with *MYC* mRNA expression and tumor purity estimation but negatively correlated with leukocyte fraction estimation (Extended Data Fig. 7j,k). Genome-wide association studies have identified numerous noncoding variants associated with increased risk of cancer. Seven SNPs associated with cancer risk map to the cancer-specific *MYC* enhancers (Extended Data Fig. 7l), including the COAD risk variant rs6983267 that has been replicated in multiple cohorts[46–50], suggesting that these variants exert

https://doi.org/10.1038/s41588-025-02188-0

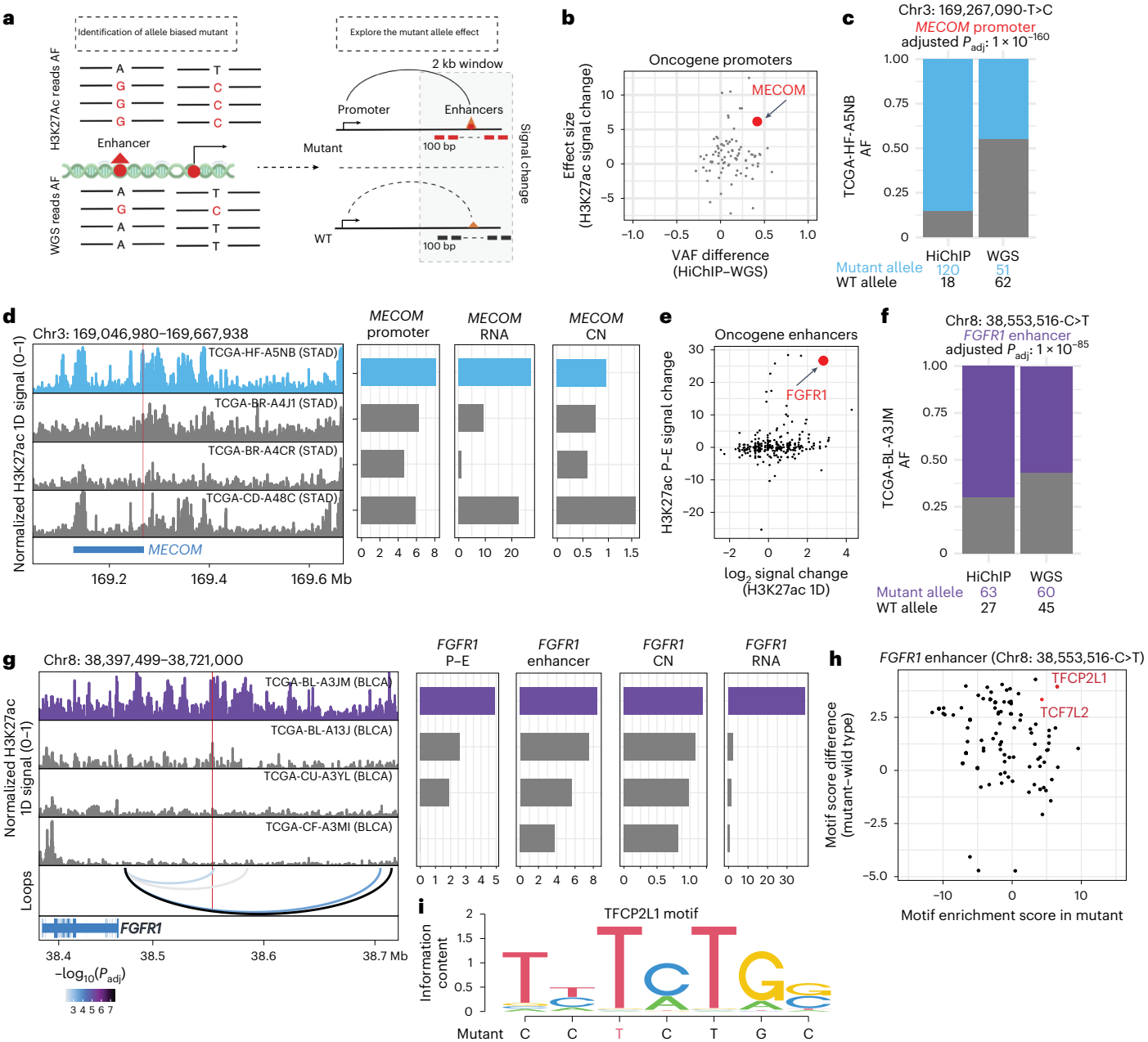

Fig. 4 | Integration of WGS and HiChIP identifies cancer-relevant regulatory mutations and target genes. a, Schematic representation showing the workflow of identifying the H3K27ac-associated noncoding mutations. **b**, Scatter plot indicating the relationship between oncogene promoter-associated HiChIP and WGS allele frequency differences and the effect size (*T* score) of the associated H3K27ac signal change between mutant and wild-type patients. The *T* score was calculated by a two-sided *t* test. **c**, Bar plot showing the allele frequency of chr3: 169,267,090-T>C (*MECOM*) mutant between HiChIP and WGS for sample TCGA-HF-A5NB (STAD). The *P* value was calculated by Fisher's exact test and corrected using the BH procedure. **d**, Signal tracks showing the integrative track of H3K27ac HiChIP at *MECOM* locus normalized by reads in TSS. The H3K27ac 1D signal track indicates the bulk level H3K27ac signal in STAD samples (left). Mutant patient TCGA-HF-A5NB is highlighted in blue. The chr3: 169,267,090-T>C mutant position is labeled in red line. Bar plots indicate matched H3K27ac signal (CN corrected), *MECOM* expression and CN at *MECOM* locus. **e**, Scatter plot quantifying the relationship between enhancer activity and enhancer–promoter interaction changes for oncogene-associated enhancers with somatic variants. **f**, Bar plot showing the allele frequency of chr8: 38,553,516-C>T (*FGFR1* enhancer) mutant between HiChIP and WGS for sample TCGA-BL-A3JM (BLCA). The *P* value was calculated by Fisher's exact test and corrected using the BH procedure. **g**, Signal tracks showing the integrative track of HiChIP 1D H3K27ac enrichment at *FGFR1* locus normalized by reads in TSS. The H3K27ac 1D signal track indicates the bulk level H3K27ac signal (CN corrected) and *FGFR1* enhancer–promoter interactions in BLCA samples (left). Mutant patient TCGA-BL-A3JM is highlighted in purple. The chr8: 38,553,516-C>T mutant position was labeled in red line. Bar plots indicate matched H3K27ac signal, *FGFR1* expression and CN at *FGFR1* locus. Significant loop interactions are colored by adjusted *P* value, and *P* values were calculated using a two-sided binomial test and corrected using the BH procedure. **h**, Scatter plot indicating the association between chr8: 38,553,516-C>T mutant-involved motif enrichment changes and motif enrichment scores in chr8: 38,553,516-C>T mutant region. **i**, Motif sequence plot showing the overlap between the mutant sequence and the enriched motif sequence for TFCP2L1. AF, allele frequency.

https://doi.org/10.1038/s41588-025-02188-0

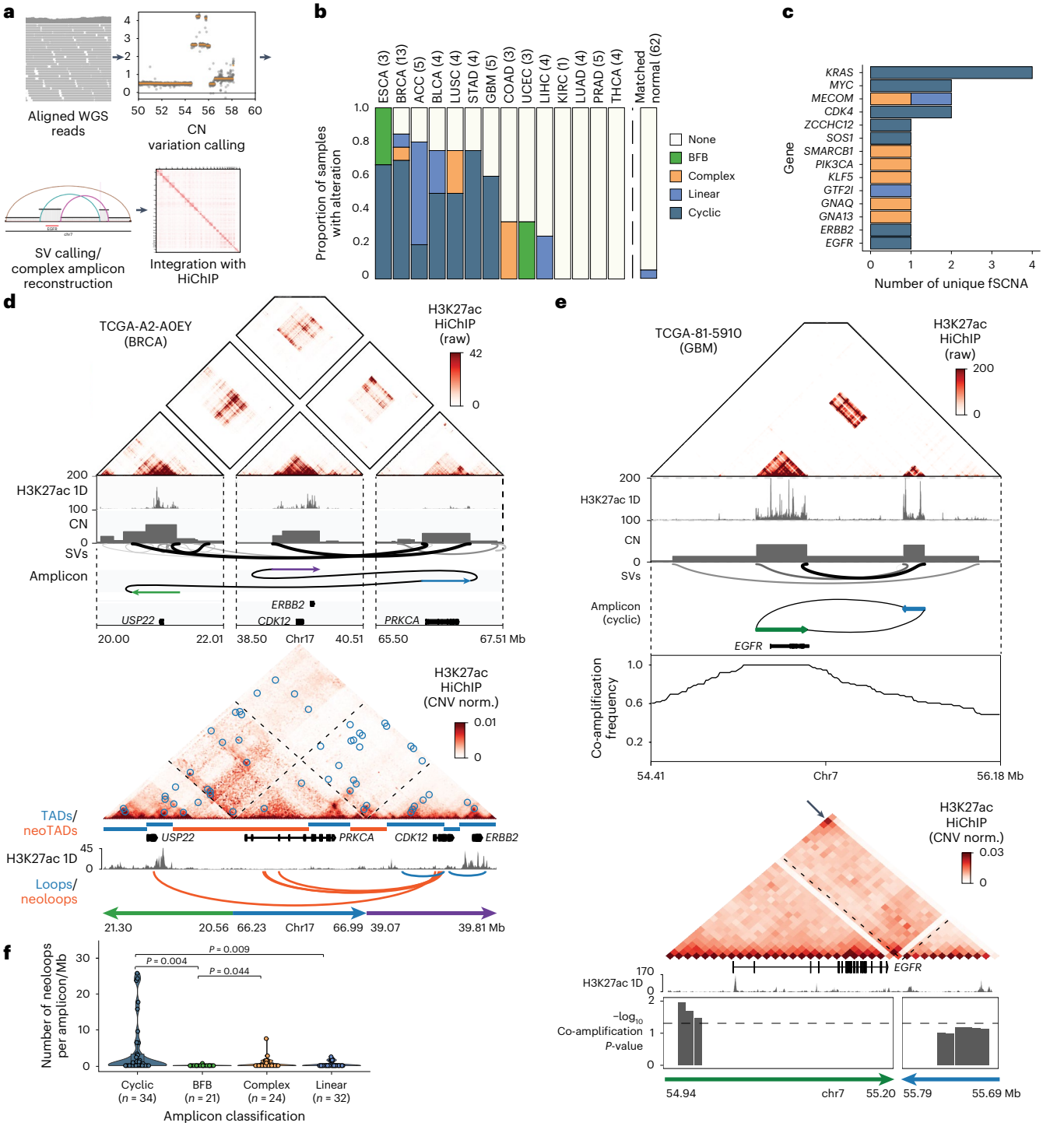

Fig. 5 | Impact of structural rearrangement and ecDNA amplification on enhancer connectivity. a, Workflow of the joint HiChIP–WGS analysis for simple structural variants and complex focal amplifications. **b**, Distribution of cyclic, BFB, complex and linear somatic focal amplifications detected across 62 tumor whole-genome samples with corresponding HiChIP data and 62 patient-matched normal samples as controls. **c**, Distribution of cyclic, BFB, complex, linear fSCNA affecting oncogenes. **d**, Raw HiChIP contact matrix of *ERBB2* rearrangement with tracks visualizing H3K27ac 1D signal enrichment, CN inferred from WGS, SVs identified by WGS and amplicon prediction (top). The raw, unnormalized HiChIP contact matrix allows for visualization of regions of high HiChIP signal before normalization, which correspond to amplifications and structural rearrangements detected by WGS. CN-normalized HiChIP contact matrix with tracks visualizing TADs/neoTADs, H3K27ac 1D signal enrichment and loops/neoloops (bottom). **e**, Raw HiChIP contact matrix of a cyclic (ecDNA-like) *EGFR* rearrangement with tracks visualizing H3K27ac 1D signal enrichment, CN inferred from WGS, SVs identified by WGS, amplicon prediction and co-amplification frequency across all TCGA WGS samples (top). Tracks visualizing H3K27ac 1D signal enrichment and significance of co-amplification with CN-normalized HiChIP matrix below (bottom). Arrow indicates increased interaction signal indicative of a circular amplicon. **f**, Violin and box plot quantifying neoloops per megabase within cyclic, BFB, complex, linear amplifications identified by NeoLoopFinder (*n* = number of unique amplifications). Loop counts are quantified for each focal amplification, normalized by the size of the focal amplification and classified as a neoloop if they span an SV breakpoint. *P* values were calculated using a two-sided Wilcoxon rank-sum test and adjusted using the BH procedure. Box centerline, median; box limits, upper and lower quartiles; box whiskers, 1.5× interquartile range. fSCNA, focal somatic CN amplifications.

their effect by impacting MYC expression in transformed cells rather than immune or stromal cells. We extend this SNP analysis to all malignant cell-specific E–P interactions, providing a comprehensive list of risk SNPs linked to target genes (Supplementary Table 7).

Three-dimensional genome reveals targets of noncoding regulatory mutations

Identification of somatic mutations in active regulatory elements with higher allele frequencies in H3K27ac HiChIP compared to WGS can nominate noncoding mutations that may promote enhancer activity to drive cancer initiation and progression (Fig. 4a). Building on prior efforts using WGS as well as ATAC–seq to nominate functional noncoding variants[12,51], additional WGS and HiChIP data generated in this study provide additional power to nominate functional variants and to identify target genes. Using somatic mutations identified by WGS, we calculated mutant allele frequencies in H3K27ac HiChIP, achieving a median correlation of 0.54 with ATAC–seq data (Extended Data Fig. 8a). We then quantified the mutant allele's impact on enhancer activity based on the average H3K27ac signal changes within a 2-kb region centered on the single-nucleotide variant relative to all cases with only the reference allele (Fig. 4a; Methods). We identified 7,517 somatic mutations (2,975 promoter mutations and 4,542 enhancer mutations) with higher variant allele frequency in H3K27ac HiChIP over WGS (Fig. 4a and Extended Data Fig. 8b; Methods), suggesting enhanced regulatory activity.

Among oncogene promoter variants, this analysis nominated a stomach cancer-associated variant (chr3: 169,267,090-T>C) in the *MECOM* promoter, showing a higher allele frequency in HiChIP (85%) than WGS (45%; Fig. 4b,c) and increased H3K27ac signal (Extended Data Fig. 8c). Furthermore, a concordant trend between H3K27ac signal changes and mRNA expression levels was observed across different patients, except for sample TCGA-CD-A48C, which had high RNA expression despite modest H3K27ac signal at the *MECOM* promoter. Examination of WGS data revealed a focal amplification of the *MECOM* locus for this sample, suggesting that either noncoding promoter mutation or gene copy amplification can promote oncogene overexpression (Fig. 4d). Indeed, *MECOM* RNA expression and H3K27ac promoter signal for the sample with the chr3: 169,267,090-T>C variant rank in the top 16% of TCGA STAD RNA-seq and top 5% of pan-cancer H3K27ac HiChIP (Extended Data Fig. 8d,e). As noncoding mutations can create new binding sites for TFs that may promote gene overexpression, we compared motif enrichment scores between *MECOM* chr3: 169,267,090-T>C mutant and wild-type sequences (Extended Data Fig. 8f). Differential motif analysis nominated AHR and FOXM1 as the most significant TF motif gained by the T>C change in the *MECOM* promoter (Extended Data Fig. 8g), and RNA-seq data analysis confirmed the expression of *AHR* and *FOXM1* in the tumor sample (Extended Data Fig. 8h).

We next investigated the presence of enhancer mutations that may impact gene expression and regulatory element activity. We first validated the previously identified *FDG4* enhancer mutation in the BLCA cohort using HiChIP (Extended Data Fig. 8i)[12]. Consistent with ATAC–seq data, the sample with the chr12: 32,385,775-C>T variant showed substantially higher H3K27ac signal compared to noncarriers (Extended Data Fig. 8i). To further nominate functional noncoding variants, we examined both 1D H3K27ac enrichment and E–P looping assessed by HiChIP and nominated 2,214 variants with increased E–P interaction signal (Extended Data Fig. 8j). The chr8: 38,553,516-C>T variant linked to the *FGFR1* promoter in BLCA exhibited allelic bias in HiChIP data and an eightfold increase in H3K27ac signal (Fig. 4e–g and Extended Data Fig. 8k). This variant dramatically enhanced E–P interaction signal (1.4- to 70-fold) and *FGFR1* expression, ranking in the top 1% of the BLCA cohort, without evidence of CNVs (Fig. 4g and Extended Data Fig. 8l). Differential motif analysis revealed that the C to T change created a new binding motif for the TFCP2L1 TF (Fig. 4h,i), which is associated with cell cycle progression and stemness during bladder cancer progression[52] and is highly expressed in the affected sample (Extended Data Fig. 8m). Finally, high *FGFR1* expression correlated with worse prognosis in BLCA, suggesting functional consequences of this enhancer-associated noncoding mutation (Extended Data Fig. 8n).

Extensive enhancer rewiring from structural rearrangements

An additional source of somatic alterations with substantial impact on 3D genome organization are structural rearrangements[19,53]. Integration of WGS analysis with H3K27ac HiChIP provides unique insight into the regulatory impact of both simple and complex structural rearrangement events, in particular focal amplifications that can promote oncogene overexpression (Fig. 5a). We first examined the regulatory impact of simple SVs identified by WGS, including deletions, duplications, inversion and translocations (Extended Data Fig. 9a). Rearranging the connectivity of DNA segments can result in both increased contact probability between two previously distant DNA segments and the formation of new TADs and new E–P loops across SV junctions. We used NeoLoopFinder to reconstruct the HiChIP interaction matrices for SVs identified by WGS, such as a translocation linking enhancers on chromosome 20 with the *PIK3R1* oncogene on chromosome 5, and identified new TADs (neoTADs) and new E–P contacts (neoloops), validating the SV reconstruction and nominating new regulatory interactions[54] (Methods; Extended Data Fig. 9b). Among all classes of simple SVs, we find that translocations tend to have higher proportion of SVs with at least one neoloop and substantially more neoloops/Mb detected per SV as well as more total loops (Extended Data Fig. 9c–e), suggesting that translocations may promote more extensive enhancer rewiring compared to other simple SV classes.

Complex rearrangements link specific amplification classes to distinct DNA repair mechanisms and regulatory features, including breakage-fusion-bridge (BFB) or translocation-bridge[55] cycles of chromosomal instability and ecDNA formation. Notably, ecDNA amplification, associated with poor clinical outcomes, drives gene overexpression through increased DNA accessibility, enhancer co-amplification and nuclear colocalization[56–59]. Focal genomic amplifications were detected from WGS data using AmpliconArchitect and classified based on the predicted connectivity of discordant breakpoints as linear, complex, cyclic (with head-to-tail connectivity characteristic of ecDNA) or BFB (Fig. 5a,b)[59–61]. Cyclic amplifications associated with ecDNA were one of the most frequent SVs among solid tumors affecting multiple oncogenes, and many tumors exhibit multiple distinct molecular species of ecDNAs (Fig. 5c and Extended Data Fig. 9f).

HiChIP data confirmed the spatial proximity of the three distal genomic segments encompassing the *ERBB2* and *CDK12* genes involved in a complex rearrangement and nominated several new E–P interactions linked to the *CDK12* gene (Fig. 5d). Predicted cyclic amplicons, such as those involving *EGFR* and *MDM2*, were further validated by increased HiChIP interaction frequency at the corner of the matrix (Fig. 5e and Extended Data Fig. 9g). Finally, regulatory elements marked by H3K27ac involved in cyclic amplicons were substantially co-amplified across the TCGA cohort based on WGS data (Fig. 5e and Extended Data Fig. 9g). In addition, we find that ecDNAs exhibit extensive sequence heterogeneity even within individual tumors. In cases where multiple amplicons were nominated by WGS, including multiple cyclic cycles involving *EGFR*, HiChIP provided orthogonal support for the dominating rearrangement, which was supported by a high interaction frequency (Fig. 5e and Extended Data Fig. 9h).

Overall, we find that different classes of rearrangements impact gene regulation at distinct scales, with ecDNA generating the largest number of new E–P loops, as well as larger overall numbers of E–P loops, compared to BFB or linear amplicons (Fig. 5f and Extended Data Fig. 9i). These findings underscore diverse mechanisms of structural rearrangements driving epigenetic rewiring in cancer.

Discussion

Here we provide an initial survey of 3D genome architecture and enhancer landscape in 15 primary human cancer types. This dataset defined chromosome topology at multiple scales and expanded the lexicon and syntax of gene regulation in cancer. Overlaying 3D genome conformation with DNA mutation, CN, single-cell chromatin accessibility and RNA expression informed how alterations in gene regulation may impact cancer. Nonetheless, due to the range of sequencing depth across archival samples, care should be taken for any pairwise comparison of 3D cancer genomes.

The genome architecture across cancer types is largely conserved in compartments and TADs but varies substantially in E–P loops. This aligns with studies across species and development, suggesting that compartments and TADs serve as stable scaffolds within which dynamic E–P loops regulate gene expression[3,23]. Focusing on driver oncogenes, we observed that CN gain and/or enhancer recruitment can lead to increased RNA expression in a gene-specific manner. Enhancer activity and rewiring better explain mRNA overexpression for most oncogenes, but for a subset, such as *KRAS*, CN gain is the dominant mechanism of overexpression. These findings may guide the clinical profiling of CNVs and regulatory element activity to identify high-risk patients and targeted therapy candidates. We identified noncoding point mutations that can create TF binding sites de novo, leading to enhancer acquisition to activate oncogenes in an allele-specific manner. Although enhancer mutations in cancer are often not recurrent across patients, they can still exhibit potent gene regulatory consequences, and the identification of functional somatic variants affecting oncogenic drivers may enable precision medicine efforts in the future.

The TME comprises a rich ecosystem of malignant and additional cell types. The integration of 3D genome data with single-cell chromatin accessibility nominated cell-type-specific E–P contacts in the TME. We found a major myeloid contribution to immune checkpoint expression, such as PD-L1, consistent with the importance of immunomodulatory tumor-associated macrophages[62]. In contrast, malignant cell-specific E–P loops intersected with SNPs that comprise the major heritable risk alleles for cancer predisposition, supporting the role of cell-autonomous mechanisms for these risk alleles.

SVs drive gene regulatory innovation in cancer by forming new E–P contacts, notably through ecDNA amplification. Unlike chromosomal SVs constrained by TADs, ecDNAs are mobile and unrestricted, driving epigenetic dysregulation and oncogene overexpression in tumor evolution[56,58,59,63,64]. Our analysis of ecDNA amplifications in TCGA samples suggests that subclonal structural rearrangements further enhance ecDNA complexity, generating new E–P loops. This aligns with findings that ecDNAs undergo enhanced mutagenesis and accelerated evolution[65] and form transcriptionally active hubs that facilitate intermolecular interactions[58,66], potentially promoting recombination upon DNA damage. As the recognition of mutated oncogenes led ultimately to targeted therapies, understanding 3D genome architecture and gene regulatory circuits may pave the way for new therapeutic strategies in the future.

Online content

Any methods, additional references, Nature Portfolio reporting summaries, source data, extended data, supplementary information, acknowledgements, peer review information; details of author contributions and competing interests; and statements of data and code availability are available at https://doi.org/10.1038/s41588-025-02188-0.

References

1. Lieberman-Aiden, E. et al. Comprehensive mapping of long-range interactions reveals folding principles of the human genome. *Science* **326**, 289–293 (2009).
2. Nora, E. P. et al. Spatial partitioning of the regulatory landscape of the X-inactivation centre. *Nature* **485**, 381–385 (2012).
3. Dixon, J. R. et al. Topological domains in mammalian genomes identified by analysis of chromatin interactions. *Nature* **485**, 376–380 (2012).
4. Lupiáñez, D. G. et al. Disruptions of topological chromatin domains cause pathogenic rewiring of gene–enhancer interactions. *Cell* **161**, 1012–1025 (2015).
5. Bintu, B. et al. Super-resolution chromatin tracing reveals domains and cooperative interactions in single cells. *Science* **362**, eaau1783 (2018).
6. Gabriele, M. et al. Dynamics of CTCF- and cohesin-mediated chromatin looping revealed by live-cell imaging. *Science* **376**, 496–501 (2022).
7. Rao, S. S. P. et al. A three-dimensional map of the human genome at kilobase resolution reveals principles of chromatin looping. *Cell* **159**, 1665–1680 (2014).
8. Dixon, J. R. et al. Chromatin architecture reorganization during stem cell differentiation. *Nature* **518**, 331–336 (2015).
9. Rubin, A. J. et al. Lineage-specific dynamic and pre-established enhancer–promoter contacts cooperate in terminal differentiation. *Nat. Genet.* **49**, 1522–1528 (2017).
10. Hsieh, T.-H. S. et al. Enhancer–promoter interactions and transcription are largely maintained upon acute loss of CTCF, cohesin, WAPL or YY1. *Nat. Genet.* **54**, 1919–1932 (2022).
11. Hoadley, K. A. et al. Cell-of-origin patterns dominate the molecular classification of 10,000 tumors from 33 types of cancer. *Cell* **173**, 291–304 (2018).
12. Corces, M. R. et al. The chromatin accessibility landscape of primary human cancers. *Science* **362**, eaav1898 (2018).
13. Javierre, B. M. et al. Lineage-specific genome architecture links enhancers and non-coding disease variants to target gene promoters. *Cell* **167**, 1369–1384 (2016).
14. Flavahan, W. A. et al. Altered chromosomal topology drives oncogenic programs in SDH-deficient GISTs. *Nature* **575**, 229–233 (2019).
15. Johnstone, S. E. et al. Large-scale topological changes restrain malignant progression in colorectal cancer. *Cell* **182**, 1474–1489 (2020).
16. Spielmann, M., Lupiáñez, D. G. & Mundlos, S. Structural variation in the 3D genome. *Nat. Rev. Genet.* **19**, 453–467 (2018).
17. Dubois, F., Sidiropoulos, N., Weischenfeldt, J. & Beroukhim, R. Structural variations in cancer and the 3D genome. *Nat. Rev. Cancer* **22**, 533–546 (2022).
18. Wu, S., Bafna, V., Chang, H. Y. & Mischel, P. S. Extrachromosomal DNA: an emerging hallmark in human cancer. *Annu. Rev. Pathol.* **17**, 367–386 (2022).
19. Akdemir, K. C. et al. Disruption of chromatin folding domains by somatic genomic rearrangements in human cancer. *Nat. Genet.* **52**, 294–305 (2020).
20. Xu, Z. et al. Structural variants drive context-dependent oncogene activation in cancer. *Nature* **612**, 564–572 (2022).
21. Dixon, J. R. et al. Integrative detection and analysis of structural variation in cancer genomes. *Nat. Genet.* **50**, 1388–1398 (2018).
22. Mumbach, M. R. et al. HiChIP: efficient and sensitive analysis of protein-directed genome architecture. *Nat. Methods* **13**, 919–922 (2016).
23. Mumbach, M. R. et al. Enhancer connectome in primary human cells identifies target genes of disease-associated DNA elements. *Nat. Genet.* **49**, 1602–1612 (2017).
24. Nasser, J. et al. Genome-wide enhancer maps link risk variants to disease genes. *Nature* **593**, 238–243 (2021).
25. Zeng, W., Liu, Q., Yin, Q., Jiang, R. & Wong, W. H. HiChIPdb: a comprehensive database of HiChIP regulatory interactions. *Nucleic Acids Res.* **51**, D159–D166 (2023).

26. Fortin, J.-P. & Hansen, K. D. Reconstructing A/B compartments as revealed by Hi-C using long-range correlations in epigenetic data. *Genome Biol.* **16**, 180 (2015).
27. Schuijers, J. et al. Transcriptional dysregulation of MYC reveals common enhancer-docking mechanism. *Cell Rep.* **23**, 349–360 (2018).
28. Dunham, I. et al. An integrated encyclopedia of DNA elements in the human genome. *Nature* **489**, 57–74 (2012).
29. Liu, Y. et al. Systematic inference and comparison of multi-scale chromatin sub-compartments connects spatial organization to cell phenotypes. *Nat. Commun.* **12**, 2439 (2021).
30. Schmitt, A. D. et al. A compendium of chromatin contact maps reveals spatially active regions in the human genome. *Cell Rep.* **17**, 2042–2059 (2016).
31. Creyghton, M. P. et al. Histone H3K27ac separates active from poised enhancers and predicts developmental state. *Proc. Natl Acad. Sci. USA* **107**, 21931–21936 (2010).
32. Rada-Iglesias, A. et al. A unique chromatin signature uncovers early developmental enhancers in humans. *Nature* **470**, 279–283 (2011).
33. Cancer Genome Atlas Research Network. et al. Integrated genomic characterization of oesophageal carcinoma. *Nature* **541**, 169–175 (2017).
34. Corces, M. R. et al. Single-cell epigenomic analyses implicate candidate causal variants at inherited risk loci for Alzheimer's and Parkinson's diseases. *Nat. Genet.* **52**, 1158–1168 (2020).
35. Bailey, M. H. et al. Comprehensive characterization of cancer driver genes and mutations. *Cell* **173**, 371–385 (2018).
36. Parolia, A. et al. Distinct structural classes of activating FOXA1 alterations in advanced prostate cancer. *Nature* **571**, 413–418 (2019).
37. Sundaram, L. et al. Single-cell chromatin accessibility reveals malignant regulatory programs in primary human cancers. *Science* **385**, eadk9217 (2024).
38. Chen, H. et al. A pan-cancer analysis of enhancer expression in nearly 9000 patient samples. *Cell* **173**, 386–399 (2018).
39. Thorsson, V. et al. The immune landscape of cancer. *Immunity* **48**, 812–830 (2018).
40. Aran, D., Sirota, M. & Butte, A. J. Systematic pan-cancer analysis of tumour purity. *Nat. Commun.* **6**, 8971 (2015).
41. Sharma, P. et al. Immune checkpoint therapy—current perspectives and future directions. *Cell* **186**, 1652–1669 (2023).
42. Oh, S. A. et al. PD-L1 expression by dendritic cells is a key regulator of T-cell immunity in cancer. *Nat. Cancer* **1**, 681–691 (2020).
43. Chen, J. C., Perez-Lorenzo, R., Saenger, Y. M., Drake, C. G. & Christiano, A. M. IKZF1 enhances immune infiltrate recruitment in solid tumors and susceptibility to immunotherapy. *Cell Syst.* **7**, 92–103 (2018).
44. Das, M., Zhu, C. & Kuchroo, V. K. Tim-3 and its role in regulating anti-tumor immunity. *Immunol. Rev.* **276**, 97–111 (2017).
45. Contardi, E. et al. CTLA-4 is constitutively expressed on tumor cells and can trigger apoptosis upon ligand interaction. *Int. J. Cancer* **117**, 538–550 (2005).
46. Zeng, C. et al. Identification of susceptibility loci and genes for colorectal cancer risk. *Gastroenterology* **150**, 1633–1645 (2016).
47. Tanikawa, C. et al. GWAS identifies two novel colorectal cancer loci at 16q24.1 and 20q13.12. *Carcinogenesis* **39**, 652–660 (2018).
48. Schumacher, F. R. et al. Genome-wide association study of colorectal cancer identifies six new susceptibility loci. *Nat. Commun.* **6**, 7138 (2015).
49. Cui, R. et al. Common variant in 6q26-q27 is associated with distal colon cancer in an Asian population. *Gut* **60**, 799–805 (2011).
50. Tanskanen, T. et al. Genome-wide association study and meta-analysis in Northern European populations replicate multiple colorectal cancer risk loci. *Int. J. Cancer* **142**, 540–546 (2018).
51. Rheinbay, E. et al. Analyses of non-coding somatic drivers in 2,658 cancer whole genomes. *Nature* **578**, 102–111 (2020).
52. Heo, J. et al. The CDK1/TFCP2L1/ID2 cascade offers a novel combination therapy strategy in a preclinical model of bladder cancer. *Exp. Mol. Med.* **54**, 801–811 (2022).
53. Li, Y. et al. Patterns of somatic structural variation in human cancer genomes. *Nature* **578**, 112–121 (2020).
54. Wang, X. et al. Genome-wide detection of enhancer-hijacking events from chromatin interaction data in rearranged genomes. *Nat. Methods* **18**, 661–668 (2021).
55. Lee, J. J.-K. et al. ERα-associated translocations underlie oncogene amplifications in breast cancer. *Nature* **618**, 1024–1032 (2023).
56. Wu, S. et al. Circular ecDNA promotes accessible chromatin and high oncogene expression. *Nature* **575**, 699–703 (2019).
57. Helmsauer, K. et al. Enhancer hijacking determines extrachromosomal circular MYCN amplicon architecture in neuroblastoma. *Nat. Commun.* **11**, 5823 (2020).
58. Hung, K. L. et al. ecDNA hubs drive cooperative intermolecular oncogene expression. *Nature* **600**, 731–736 (2021).
59. Kim, H. et al. Extrachromosomal DNA is associated with oncogene amplification and poor outcome across multiple cancers. *Nat. Genet.* **52**, 891–897 (2020).
60. Deshpande, V. et al. Exploring the landscape of focal amplifications in cancer using AmpliconArchitect. *Nat. Commun.* **10**, 392 (2019).
61. Turner, K. M. et al. Extrachromosomal oncogene amplification drives tumor evolution and genetic heterogeneity. *Nature* **543**, 122–125 (2017).
62. Cheng, S. et al. A pan-cancer single-cell transcriptional atlas of tumor infiltrating myeloid cells. *Cell* **184**, 792–809 (2021).
63. Hung, K. L., Mischel, P. S. & Chang, H. Y. Gene regulation on extrachromosomal DNA. *Nat. Struct. Mol. Biol.* **29**, 736–744 (2022).
64. Luebeck, J. et al. Extrachromosomal DNA in the cancerous transformation of Barrett's oesophagus. *Nature* **616**, 798–805 (2023).
65. Bergstrom, E. N. et al. Mapping clustered mutations in cancer reveals APOBEC3 mutagenesis of ecDNA. *Nature* **602**, 510–517 (2022).
66. Yi, E. et al. Live-cell imaging shows uneven segregation of extrachromosomal DNA elements and transcriptionally active extrachromosomal DNA hubs in cancer. *Cancer Discov.* **12**, 468–483 (2022).

[1]Center for Personal Dynamic Regulomes, Stanford University School of Medicine, Stanford, CA, USA. [2]Department of Dermatology, Stanford University School of Medicine, Stanford, CA, USA. [3]Department of Genetics, Stanford University School of Medicine, Stanford, CA, USA. [4]Department of Computer Science and Engineering, University of California, San Diego, La Jolla, CA, USA. [5]Sandra and Edward Meyer Cancer Center, Weill Cornell Medicine, New York City, NY, USA. [6]Department of Physiology and Biophysics, Weill Cornell Medicine, New York City, NY, USA. [7]Gladstone Institute of Neurological Disease, San Francisco, CA, USA. [8]Gladstone Institute of Data Science and Biotechnology, San Francisco, CA, USA. [9]Department of Neurology, University of California, San Francisco, San Francisco, CA, USA. [10]Broad Institute of MIT and Harvard, Cambridge, MA, USA. [11]Department of Computer Science, Stanford University, Stanford, CA, USA. [12]Illumina AI laboratory, Illumina Inc, Foster City, CA, USA. [13]NVIDIA Bio Research, NVIDIA, Santa Clara, CA, USA. [14]Vilcek Institute of Graduate Biomedical Sciences, NYU Grossman School of Medicine, New York City, NY, USA. [15]Laura and Isaac Perlmutter Cancer Center, New York University Langone Health, New York City, NY, USA. [16]Department of Pathology, New York University Langone Health, New York City, NY, USA. [17]New York Genome Center, New York City, NY, USA. [18]Department of Pathology and Laboratory Medicine, Weill Cornell Medicine, New York City, NY, USA. [19]Department of Biochemistry, Faculty of Science, Cancer and Mutagenesis Unit, King Fahd Center for Medical Research, King Abdulaziz University, Jeddah, Saudi Arabia. [20]Department of Medical Oncology, Dana–Farber Cancer Institute, Boston, MA, USA. [21]Harvard Medical School, Boston, MA, USA. [22]Institute for Computational Biomedicine, Weill Cornell Medicine, New York City, NY, USA. [23]Englander Institute for Precision Medicine, Weill Cornell Medicine, New York City, NY, USA. [24]National Cancer Institute, NIH, Bethesda, MD, USA. [25]Center for Epigenetics, Van Andel Research Institute, Grand Rapids, MI, USA. [26]Department of Medicine, Stanford University School of Medicine, Stanford, CA, USA. [27]Chan Zuckerberg Biohub, San Francisco, CA, USA. [28]Department of Applied Physics, Stanford University, Stanford, CA, USA. [29]Howard Hughes Medical Institute, Stanford University School of Medicine, Stanford, CA, USA. [30]Present address: Pathos AI, Chicago, IL, USA. [31]Present address: Whitehead Institute for Biomedical Research, Cambridge, MA, USA. [32]These authors contributed equally: Kathryn E. Yost, Yanding Zhao. *A list of authors and their affiliations appear at the end of the paper.
✉e-mail: wjg@stanford.edu; howchang@stanford.edu

Cancer Genome Atlas Analysis Network

Kathryn E. Yost[1,2,31,32], Yanding Zhao[1,2,3,32], King L. Hung[1,2], Kaiyuan Zhu[4], Duo Xu[5,6,30], M. Ryan Corces[7,8,9], Shahab Sarmashghi[10], Laksshman Sundaram[3,11,12,13], Jens Luebeck[4], Ashley S. Doane[18], Jeffrey M. Granja[1,2,3], Andrew D. Cherniack[10,20,21], Ekta Khurana[5,6,22,23], Vineet Bafna[4], Ina Felau[24], Jean C. Zenklusen[24], Peter W. Laird[25], Christina Curtis[3,26,27], William J. Greenleaf[3,28] & Howard Y. Chang[1,2,29]

Methods

Ethical approval

This study complied with all relevant ethical regulations and ethical guidance was overseen by the TCGA Program Office. Each study site that contributed biological material had its own ethics board approval. TCGA ethics policies are available at https://www.cancer.gov/ccg/research/genome-sequencing/tcga/history/ethics-policies.

Tumor sample selection

Samples were selected from the set of samples previously profiled by bulk ATAC–seq[12] to span the 15 cancer types profiled in this manuscript, with a focus on breast cancer and at least three samples for each other cancer. Within breast cancer, three samples were selected from each major breast cancer subtype (Basal, HER2, LumA and LumB).

Statistics and reproducibility

Samples were prioritized for selection based on high data quality in previous bulk ATAC–seq experiments, the availability of sufficient nuclei in cryopreserved stocks and the representation of the diversity of cancer types profiled by TCGA. No statistical method was used to predetermine sample size. No data were excluded from the analyses. The experiments were not randomized. The investigators were not blinded to allocation during experiments and outcome assessment. Data distribution was assumed to be normal, but this was not formally tested.

HiChIP library generation

HiChIP library generation was performed following published protocols[22]. Nuclei used for HiChIP were isolated as part of a previous study[12] and cryopreserved in BAM Banker. One million cryopreserved nuclei were used per experiment. Briefly, enzyme MboI was used for restriction digestion. Sonication was performed on a Covaris E220 instrument using the following settings: duty cycle 5, peak incident power 140, cycles per burst 200 and time 4 min. All HiChIP was performed using H3K27ac as the target (Abcam, ab4729). Libraries were sequenced on an Illumina HiSeq 4000 with paired-end 75 bp reads. Full protocol details are described in Supplementary Methods.

Preparation of WGS libraries for cluster amplification and sequencing

In total, 268 TCGA tumor samples were profiled by deep WGS sequencing in this study, and for 263 matched normal samples, WGS was also generated for identification of somatic variants, either collected from peripheral blood ($n = 255$) or from adjacent normal tissue ($n = 8$). Five tumor samples profiled by WGS in this study had previously generated WGS data from normal blood or tissue, which was used in somatic variant identification (Supplementary Table 2). An aliquot of genomic DNA (350 ng in 50 µl) is used as the input into DNA fragmentation (also known as shearing). Shearing is performed acoustically using a Covaris focused-ultrasonicator, targeting 385-bp fragments. Following fragmentation, additional size selection is performed using a solid-phase reversible immobilization cleanup. Library preparation is performed using a commercially available kit provided by KAPA Biosystems (KAPA Hyper Prep without amplification module, KK8505) and with palindromic forked adapters with unique eight-base index sequences embedded within the adapter (purchased from Roche, KK8727). Libraries were sequenced on an Illumina NovaSeq 6000 with paired-end 151-bp reads.

HiChIP data analysis

HiChIP data were processed as described previously[22]. In brief, paired-end reads were aligned to the hg38 genome using the HiC-Pro pipeline (v.2.11.0)[67]. Default settings were used to remove duplicate reads, assign reads to MboI restriction fragments, filter for valid interactions and generate binned interaction matrices. FitHiChIP (v.8.0) was used to identify loops[68]. Dangling end, self-circularized and religation read pairs were merged with valid read pairs to create a 1D H3K37ac signal bed file, corresponding to H3K27ac ChIP followed by sequencing (ChIP–seq)-like signal that was used for peak calling and 1D signal quantification using standard ChIP–seq analysis tools, including MACS2. FitHiChIP was used to identify 'peak-to-all' interactions at 10-kb resolution using peaks called from the 1D HiChIP data using MACS2 (ref. 69). Loop calling was restricted to loops with anchors on the same chromosome and separated by 40 kb to 2 Mb. Bias correction was performed using coverage-specific bias. HiChIP loop calling was performed at 10-kb resolution to balance resolution for identifying relevant E–P interactions with sensitivity in loop calling, which improves at lower resolutions. Per-sample loop calling generated, on average, 112,081 unique interactions per sample, ranging from 580 to 436,780. Filtered read pairs from the HiC-Pro pipeline were converted into .hic format files for visualization and normalization[70].

WGS analysis

WGS reads were aligned to the hg38 genome using BWA-MEM, and variants were called using the Genomic Data Commons (GDC)/Sanger WGS Variant Calling pipeline (https://docs.gdc.cancer.gov/Data/Bioinformatics_Pipelines/DNA_Seq_Variant_Calling_Pipeline/#whole-genome-sequencing-variant-calling)[71]. Briefly, SNV calls were generated with CaVEMan[72], small insertions/deletions were identified using Pindel[73], structural variants were identified using BRASS (https://github.com/cancerit/BRASS) and somatic CN alterations were identified using AscatNGS[74]. WGS read depth statistics were generated using mosdepth (v.0.3.1)[75]. We performed quality control on CN calls (CNVs) generated using the ASCAT pipeline by comparing them with manually reviewed calls from running the ABSOLUTE pipeline on SNP array data. ASCAT does not explicitly output ploidies, so we calculated its estimated ploidy by averaging the total CN of segments weighted by their lengths. For most samples, we observed concordant estimates from both pipelines, and further normalizing CNs by estimated ploidies resolved the majority of discordances. These ploidy-normalized values are used to compare the contribution of CNs to the gene expression across tumors with different ploidy levels. We also examined calls to detect high levels of noise by counting the number of segments and used 1,000 segments to identify hyper-segmented samples. Four samples with associated HiChIP data surpassed this cutoff and were excluded from further analysis. These four samples were associated with cases for which multiple WGS sequencing libraries were generated, and the other WGS library was used for subsequent analysis. To assess the consistency of WGS CNV calls with prior studies, we determined the proportion of cases within each cancer type with either CNV gain ($>1\log_2$(ploidy-corrected CNV)) or CNV loss ($<-1\log_2$(ploidy-corrected CNV)) in 1 Mb genomic windows.

HiChIP interaction annotation

We annotated significant HiChIP interactions identified by FitHiChIP based on overlap with gene promoters and/or enhancers. First, we intersected FitHiChIP loop anchors with gene promoters obtained from TxDb.Hsapiens.UCSC.hg38.knownGene (v.3.10.0) and extended by ±1 kb. Anchors that did not overlap with a gene promoter were then intersected with the union H3K27ac peak set to identify anchors that overlap with putative enhancers. HiChIP interactions were then annotated as either E–P, enhancer–enhancer (E–E), promoter–promoter (P–P), enhancer–neither (E–N) or promoter–neither (P–N). Loop classifications were based on annotation of loop anchors, with loop anchors annotated as promoter if they overlapped the promoter (±1 kb of annotated TSS) of at least one gene, enhancer if they overlapped with an H3K27ac peak and no promoters, and neither if they did not overlap with a promoter or H3K27ac peak.

Interaction matrix visualization

Two-dimensional interaction matrices were visualized using Juicebox (v.1.11.08) or with the plotgardener package in R (v.1.2.10)[76].

Eigenvector calculation and A/B compartment annotation

The eigenvector (first principal component of Pearson's matrix) for H3K27ac HiChIP observed/expected interaction matrices was obtained from .hic files using juicer_tools eigenvector function (v.1.9.9) at 500-kb resolution with Knight–Ruiz (KR) normalization. The sign of the eigenvector and A/B compartment annotation was assigned based on correlation with DNA methylation eigenvector and compartment analysis obtained from additional file 2 of ref. 26. A positive eigenvector sign is used to indicate A (open) compartment and a negative sign to indicate B (closed) compartment, the opposite of the eigenvector sign convention used in ref. 26, and thus the eigenvector sign is flipped relative to the sign in ref. 26.

H3K27ac 1D signal and virtual 4C visualization

One-dimensional H3K27ac enrichment and ATAC–seq signal were visualized following normalization by reads in TSS regions as described in the ArchR package[77]. ATAC–seq signal tracks were obtained from the GDC publication page[12]. H3K27ac ChIP–seq signal tracks were obtained from ENCODE (accessions ENCFF905FLR and ENCFF873MWG)[28,78]. Virtual 4C plots were generated from dumped matrices generated with Juicer Tools (1.9.9). The Juicer Tools tools dump command was used to extract the chromosome of interest from the .hic file. The interaction profile of a 10-kb bin containing the anchor was then plotted in R (v.4.0.3) after normalization by the total number of valid read pairs and smoothing with the rollmean function from the zoo package (v.1.8-9).

Generation of union H3K27ac peak and interaction count matrices

One-dimensional H3K27ac peaks called by MACS2 were merged using bedtools merge, and peak signal was calculated using bedtools coverage using 1D H3K27ac signal bed files (v2.28.0). Significant HiChIP interactions identified by FitHiChIP were merged using FitHiChIP's CombineNearbyInteraction.py, and the loop signal was calculated using pgltools coverage (v.2.2.0)[79]. Raw peak and loop signal were normalized using DESeq2's size factors normalization obtained using counts(dds,normalized = TRUE) (v.1.30.1)[80]. CNV correction was performed for cases with matching WGS data by dividing normalized signal by ploidy-corrected relative CNV values for peaks or loops overlapping with amplified genomic intervals (relative CNV > 1). Peaks or loops that overlapped genomic intervals with CNV equal to zero or no CNV call were converted to NA values for those samples. For CNV correction of 2D loop signal, the relative CNV value of each loop anchor was determined, and the normalized loop signal was divided by the product of the CNV values at the two anchors. Seven samples did not have matched WGS data for CNV correction and were excluded from further analysis.

Unsupervised hierarchical clustering and cluster purity calculation

For hierarchical clustering in Fig. 1f, we used CALDER[29] (v.2.0) to obtain subcompartment calls at 10-kb resolution and performed clustering using vectorized subcompartment annotations based on the compartment rank annotation returned by CALDER. Pairwise Pearson correlations were calculated using the cor function in R using 'pairwise.complete.obs'. Heatmap visualization and hierarchical clustering were performed using the pheatmap function in R (v.1.0.12). Clustering assignments were obtained using the cutree function in R with k equal to the number of unique cancer types. Clustering purity and entropy were calculated using the purity and entropy functions from the NMF package in R (v.0.26)[81].

For 1D H3K27ac and loop signal clustering, pairwise Pearson correlations were calculated using the normalized, CN-corrected count matrices. Peaks and loops on chrX and chrY and those overlapping hg38 blacklist regions[82] (https://github.com/Boyle-Lab/Blacklist/blob/master/lists/hg38-blacklist.v2.bed.gz) were excluded from analysis. Correlation analysis was performed on reproducible peaks and loops where at least two samples had a normalized count value ≥3. Count matrices were $\log_2$-transformed using a prior count of 1 to reduce the contribution of variance from elements with low count values and to avoid taking the log of zero. Visualization, clustering and purity calculations were performed as described above.

Modeling of oncogene expression with CN and enhancer activity

To determine the relative contributions of CN and enhancer activity to variability in oncogene expression, we integrated H3K27ac peaks and interactions, WGS ploidy-corrected CNV calls and HTSeq counts from RNA-seq data for annotated gene loci. Samples missing from any of these datasets were excluded from this analysis. RNA-seq raw counts were normalized using DESeq2's size factors normalization obtained using counts(dds,normalized = TRUE) (v.1.26.0). Union H3K27ac peaks within 1 Mb away from annotated gene TSSs that were supported by peak–TSS interaction loops in HiChIP were considered. To account for increased HiChIP read counts due to CNV, read counts of these TSS-associated H3K27ac peaks were normalized to ploidy-corrected CNs as follows: CNV-normalized peak count = (DESeq2-normalized peak count)/(ploidy-corrected CN × 2 + 1). To assess the variability in gene expression, we first filtered on expressed genes defined as genes with more than ten transcripts per million in more than three samples in the RNA-seq dataset. We then used multiple linear regression to model the DESeq2-normalized RNA-seq gene expression values using the formula RNA ~ H3K27ac + CN, where RNA is the DESeq2-normalized RNA-seq gene expression value, H3K27ac represents terms of $\log_2$-transformed, scaled and centered 1D H3K27ac counts of peaks associated with the given gene and CN represents the ploidy-corrected CN of the gene. For genes with which more than five H3K27ac peaks were associated, $\log_2$-transformed, scaled and centered 1D H3K27ac counts were reduced to five principal components using the pca function in R with ncomp = 5, center = TRUE, scale = TRUE. For genes with five or less linked H3K27ac peaks, individual peak signal was used as input for RNA expression modeling rather than PCs. Relative importance of model predictors for each gene was quantified with the Lindeman, Merenda and Gold (LMG) method using the calc.relimp function in R with type = 'lmg', rela = FALSE. To analyze the relative importance of H3K27ac HiChIP signal and CN of oncogenes, we curated a list of oncogenes and possible oncogenes based on previous analysis[35]. $\log_2$ transformation of count data was performed as $\log_2$(count + 1) unless specified otherwise.

Sample-specific scATAC–seq data analysis

The processed scATAC–seq ArchR object (v1.0.1) with cell-type annotation was obtained from the associated publication[37]. For each sample with matched H3K27ac HiChIP data, we regenerated ArchR object and recalculated chromatin accessibility peaks for each cell population through MACS2 (v2.1.1) under default setting.

HiChIP integration with scATAC–seq

In total, 29 samples with matched H3K27ac HiChIP and scATAC–seq data were used. A minimum number of 110 noncancer cells was required in each sample to ensure the power of scATAC–seq peak signal detection in the TME, which ends up with 16 samples for integration. For each matched sample, we examined the co-occurrence of H3K27ac peaks and scATAC–seq peaks in the anchor regions of enhancer–promoter interactions. The cell-type-specific enhancer–promoter interaction was identified when (1) the promoter region of the regulated gene had both H3K27ac and scATAC–seq peaks and (2) the enhancer region defined by the HiChIP interactions had H3K27ac peaks but was uniquely accessible in a specific cell type. The cell type shared enhancer–promoter interaction was defined when the promoter or enhancer regions had both H3K27ac and scATAC–seq peaks but were not limited to a specific cell type. The ambiguous enhancer–promoter interaction

was defined when both promoter and enhancer region could not map to any scATAC peaks. To generalize our sample-specific analysis to the broader population, we performed a correlation analysis between the enhancer–promoter interaction signal and the corresponding cell fraction in the TME. We obtained these cell fractions from scATAC–seq and estimated leukocyte fractions from RNA-seq data. The Spearman correlation coefficient (Rho) was calculated for each correlation, and we applied cutoff values of Rho ≥0.30 and Rho ≥0.25 to filter the results. For validation of H3K27ac HiChIP deconvolution in TME, the RNA-seq-derived leukocyte fraction estimation, ImmuneScore and tumor purity estimation were downloaded, respectively, from the original publication for correlation analysis[39,40,83].

Identification of noncoding mutation involved H3K27ac modification

In total, 62 samples with matched H3K27ac HiChIP and WGS data were used. We used the somatic mutation calling from WGS data as the ground truth. The mutation allele frequency of H3K27ac HiChIP data was generated using bcfools. First, the globally aligned H3K27ac BAM files from the FitHiChIP pipeline were piled up through the mpileup function from bctools (v1.17). Then, the derived BCF files were converted into VCF files through the call function from bcftools. The allele frequency of each somatic mutation was quantified from the VCF files accordingly. The read coverage of H3K27ac HiChIP at the somatic mutation site was calculated through multiBamSummary from deeptools. To ensure accurate allele frequency estimations, we filtered somatic mutations with read counts >30 in both WGS and H3K27ac HiChIP. The significance of the mutant allele was estimated using Fisher's exact test, followed by the Benjamini–Hochberg (BH) method for multiple comparison correction.

The H3K27ac signal change involved in the mutation site was quantified using the 2-kb window that centered at the mutation position. The 2-kb window was split into 20 bins, with each bin equal to 100 bp. The H3K27ac HiChIP signal was calculated through multiBamSummary from deeptools (v2.0) and normalized by the library size and CN. For each mutation, we performed *t* test between mutant samples and wild-type samples to quantify the difference in CNV-corrected H3K27ac signals. To perform multiple comparison correction, we used the BH method.

Quantification of noncoding mutation involved motif enrichment changes

chromVARmotifs R package (v0.2) was used for the collection of human TF binding motifs. motifmatchr R package was used for performing motif enrichment analysis. First, a 21-bp sequence centered at mutation position was derived. Then, the matchMotifs function was applied to the 21 bp sequences from mutant and wild type for motif enrichment calculation under the parameter out = 'positions' with a *P* value cutoff of 0.01.

AmpliconArchitect reconstruction of complex structural rearrangements

We collected 120 tumor WGS samples from 15 distinct cancer types and 123 matched normal WGS samples from TCGA, all aligned to GRCh38. We ran AmpliconSuite v.0.931.4 (https://github.com/AmpliconSuite/AmpliconSuite-pipeline), which invoked CNVkit[84] to call genome-wide CN profiles and identify seed amplicon intervals with CN values larger than 4.5 from these aligned WGS samples. We then ran AmpliconArchitect[60] v,1.3_r1 to infer the structure of focal amplifications from each sample, with the aligned WGS reads and seed amplicon intervals as input. AmpliconArchitect was run with parameters -insert_sdevs 9 to filter artifactual discordant reads and improve runtime performance and default parameters otherwise. Focal amplifications were classified as cyclic, BFB, complex, linear or invalid using AmpliconClassifier v.0.4.10 (https://github.com/AmpliconSuite/AmpliconClassifier).

HiChIP visualization at structural rearrangements with NeoLoopFinder

We ran NeoLoopFinder[54] v.0.2.5 to search for chromatin loops on rearranged genomes (corresponding to local assemblies of linked breakpoints) and CN-corrected H3K27ac HiChIP matrices. Input cool files were generated at 10-kb resolution from .hic files using HiCExplorer's hicConvertFormat (v.2.2) and balanced using cooler balance (v.0.9.1). ASCAT CNV calls were used for CNV correction using NeoLoopFinder's correct-cnv, and BRASS SVs were used for complex SV assembly with NeoLoopFinder's assemble-complexSVs and supplemented with local assemblies from AmpliconArchitect cycle decomposition. Neoloops were detected using neoloop-caller -O neo-loops.txt allValidPairs.cool --assembly assemblies.txt --balance-type CNV --protocol insitu --prob 0.95 --nproc 20.

Reporting summary

Further information on research design is available in the Nature Portfolio Reporting Summary linked to this article.

Data availability

Processed data not provided in the supplementary data files are available through the TCGA Publication Page (https://gdc.cancer.gov/about-data/publications/TCGA-HiChIP-2024). Raw HiChIP data as fastq files are available through the NIH Genomic Data Commons portal (https://portal.gdc.cancer.gov/), and accession information is available on the TCGA Publication Page.

Code availability

Custom code used in this study is available at https://github.com/NCIC-CGPO/HiChIP-Manuscript and via Zenodo at https://doi.org/10.5281/zenodo.15103075 (ref. 85).

References

67. Servant, N. et al. HiC-Pro: an optimized and flexible pipeline for Hi-C data processing. *Genome Biol.* **16**, 259 (2015).
68. Bhattacharyya, S., Chandra, V., Vijayanand, P. & Ay, F. Identification of significant chromatin contacts from HiChIP data by FitHiChIP. *Nat. Commun.* **10**, 4221 (2019).
69. Zhang, Y. et al. Model-based analysis of ChIP–seq (MACS). *Genome Biol.* **9**, R137 (2008).
70. Rao, S. S. P. et al. A 3D map of the human genome at kilobase resolution reveals principles of chromatin looping. *Cell* **159**, 1665–1680 (2014).
71. Grossman, R. L. et al. Toward a shared vision for cancer genomic data. *N. Engl. J. Med.* **375**, 1109–1112 (2016).
72. Jones, D. et al. cgpCaVEManWrapper: simple execution of CaVEMan in order to detect somatic single nucleotide variants in NGS data. *Curr. Protoc. Bioinformatics* **56**, 15.10.1–15.10.18 (2016).
73. Raine, K. M. et al. cgpPindel: identifying somatically acquired insertion and deletion events from paired end sequencing. *Curr. Protoc. Bioinformatics* **52**, 15.7.1–15.7.12 (2015).
74. Raine, K. M. et al. ascatNgs: identifying somatically acquired copy-number alterations from whole-genome sequencing data. *Curr. Protoc. Bioinformatics* **56**, 15.9.1–15.9.17 (2016).
75. Pedersen, B. S. & Quinlan, A. R. Mosdepth: quick coverage calculation for genomes and exomes. *Bioinformatics* **34**, 867–868 (2018).
76. Kramer, N. E. et al. Plotgardener: cultivating precise multi-panel figures in R. *Bioinformatics* **38**, 2042–2045 (2022).
77. Granja, J. M. et al. ArchR is a scalable software package for integrative single-cell chromatin accessibility analysis. *Nat. Genet.* **53**, 403–411 (2021).
78. Luo, Y. et al. New developments on the encyclopedia of DNA elements (ENCODE) data portal. *Nucleic Acids Res.* **48**, D882–D889 (2020).

79. Greenwald, W. W. et al. Pgltools: a genomic arithmetic tool suite for manipulation of Hi-C peak and other chromatin interaction data. *BMC Bioinformatics* **18**, 207 (2017).
80. Love, M. I., Huber, W. & Anders, S. Moderated estimation of fold change and dispersion for RNA-seq data with DESeq2. *Genome Biol.* **15**, 550 (2014).
81. Gaujoux, R. & Seoighe, C. A flexible R package for nonnegative matrix factorization. *BMC Bioinformatics* **11**, 367 (2010).
82. Amemiya, H. M., Kundaje, A. & Boyle, A. P. The ENCODE blacklist: identification of problematic regions of the genome. *Sci. Rep.* **9**, 9354 (2019).
83. Yoshihara, K. et al. Inferring tumour purity and stromal and immune cell admixture from expression data. *Nat. Commun.* **4**, 2612 (2013).
84. Talevich, E., Shain, A. H., Botton, T. & Bastian, B. C. CNVkit: genome-wide copy number detection and visualization from targeted DNA sequencing. *PLoS Comput. Biol.* **12**, e1004873 (2016).
85. Zhao, Y. & Yost, K. katieyost/HiChIP-manuscript: v1.0.0. *Zenodo* https://doi.org/10.5281/zenodo.15103075 (2025).
86. Curtis, C. et al. The genomic and transcriptomic architecture of 2000 breast tumours reveals novel subgroups. *Nature* **486**, 346–352 (2012).
87. Ally, A. et al. Comprehensive and integrative genomic characterization of hepatocellular carcinoma. *Cell* **169**, 1327–1341 (2017).
88. Koboldt, D. C. et al. Comprehensive molecular portraits of human breast tumours. *Nature* **490**, 61–70 (2012).
89. The Cancer Genome Atlas Research Network. Comprehensive genomic characterization of squamous cell lung cancers. *Nature* **489**, 519–525 (2012).
90. Tonon, G. et al. High-resolution genomic profiles of human lung cancer. *Proc. Natl Acad. Sci. USA* **102**, 9625–9630 (2005).
91. Sanchez-Vega, F. et al. Oncogenic signaling pathways in The Cancer Genome Atlas. *Cell* **173**, 321–337 (2018).

Acknowledgements

This work was supported by R35-CA209919 (to H.Y.C.), RM1-HG007735 (to H.Y.C. and W.J.G.), R01NS128028 (to W.J.G.), R01HL171611 (to W.J.G.), DP1HG013599 (to W.J.G.) and an International Cooperation Award (to H.Y.C. and H.C.). This work was delivered as part of the eDyNAmiC team, supported by the Cancer Grand Challenges partnership funded by Cancer Research UK (grants CGCSDF-2021\100007 to H.Y.C. and CGCATF-2021/100025 to V.B.) and the National Cancer Institute (OT2CA278635 to V.B.). It was supported in part by the National Institutes of Health (NIH; grants U24CA264379 and R01GM114362 to V.B., and U24CA264032 and R01CA218668 to E.K.) and by WorldQuant Foundation (to E.K.). Additional support was provided through the NIH Genomic Data Analysis Networks: 1U24CA264029-01 to R. Beroukhim (Dana-Farber Cancer Institute, Harvard Medical School) and A.D.C., 1U24CA264023-01 to P.W.L., 1U24CA264032-01 to O. Elemento (Weill Cornell Medicine), 1U24CA264021-01 to K. Hoadley (University of North Carolina at Chapel Hill) and 1U24CA264009-01 to J.M. Stuart (University of California, Santa Cruz). H.Y.C. is an investigator of the Howard Hughes Medical Institute. W.J.G. is an Arc Innovation Investigator. K.L.H. was supported by a Stanford Graduate Fellowship and a National Cancer Institute (NCI) Predoctoral to Postdoctoral Fellow Transition Award (NIH F99CA274692). K.E.Y. was supported by the National Science Foundation Graduate Research Fellowship Program (NSF DGE-1656518), a Stanford Graduate Fellowship and an NCI Predoctoral to Postdoctoral Fellow Transition Award (NIH F99CA253729).

Author contributions

H.Y.C. and W.J.G. conceived of and designed the study. K.E.Y. and Y.Z. performed data analysis unless noted otherwise, compiled figures and wrote the paper with the help of all authors. S. Shams, B.H.L. and M.R.C. performed all tissue processing and HiChIP data generation. M.R.C. and J.M.G. wrote the HiChIP data processing pipeline and M.R.C. processed all HiChIP data. K.E.Y. performed HiChIP data quality control analysis, annotation of HiChIP interaction analysis, HiChIP visualization analysis, clustering analysis and HiChIP visualization at structural rearrangements. Y.Z. performed HiChIP genotype correlation analysis, feature binarization analysis with input from M.R.C., integration with scATAC–seq data with input from L.S. and identification of noncoding variants. K.L.H. performed oncogene expression modeling analysis. K.Z. performed reconstruction of complex structural arrangements analysis, neoloop analysis and co-amplification frequency analysis with input from J.L., V.B., S.C., A.S.D. and M.I. D.X. performed enhancer rewiring analysis with input from E.K. S. Sarmashghi performed ploidy normalization of WGS CNV calls with input from A.D.C. H.Y.C., W.J.G., M.R.C., J.C.Z., V.B., E.K., A.D.C., H.C. and C.C. guided data analysis. I.F. coordinated all TCGA analysis working group efforts. J.C.Z. selected tumor samples to profile in this study. H.Y.C., W.J.G. and P.W.L. cochaired the TCGA analysis working group.

Competing interests

H.Y.C. is a cofounder of Accent Therapeutics, Boundless Bio, Cartography Biosciences and Orbital Therapeutics; was an advisor of 10x Genomics, Arsenal Biosciences, Chroma Medicine and Spring Discovery until 15 December 2024 and is an employee and stockholder of Amgen as of 16 December 2024. K.E.Y. is a consultant for Cartography Biosciences. A.D.C. receives research funding from Bayer and is a consultant for KaryoVerse. P.W.L. is an advisor for Tagomics, FOXO Biosciences and AnchorDX. W.J.G. is named as an inventor on patents describing ATAC–seq methods. 10x Genomics has licensed intellectual property on which W.J.G. is listed as an inventor. W.J.G. holds options in 10x Genomics and is a consultant for Ultima Genomics and Guardant Health. W.J.G. is a scientific cofounder of Protillion Biosciences. V.B. is a cofounder, serves on the scientific advisory board of Boundless Bio and Abterra and holds equity in both companies. The other authors declare no competing interests.

Additional information

Extended data is available for this paper at https://doi.org/10.1038/s41588-025-02188-0.

Supplementary information The online version contains supplementary material available at https://doi.org/10.1038/s41588-025-02188-0.

Correspondence and requests for materials should be addressed to William J. Greenleaf or Howard Y. Chang.

Peer review information *Nature Genetics* thanks Kadir Akdemir, Feng Yue and the other, anonymous, reviewer(s) for their contribution to the peer review of this work.

https://doi.org/10.1038/s41588-025-02188-0

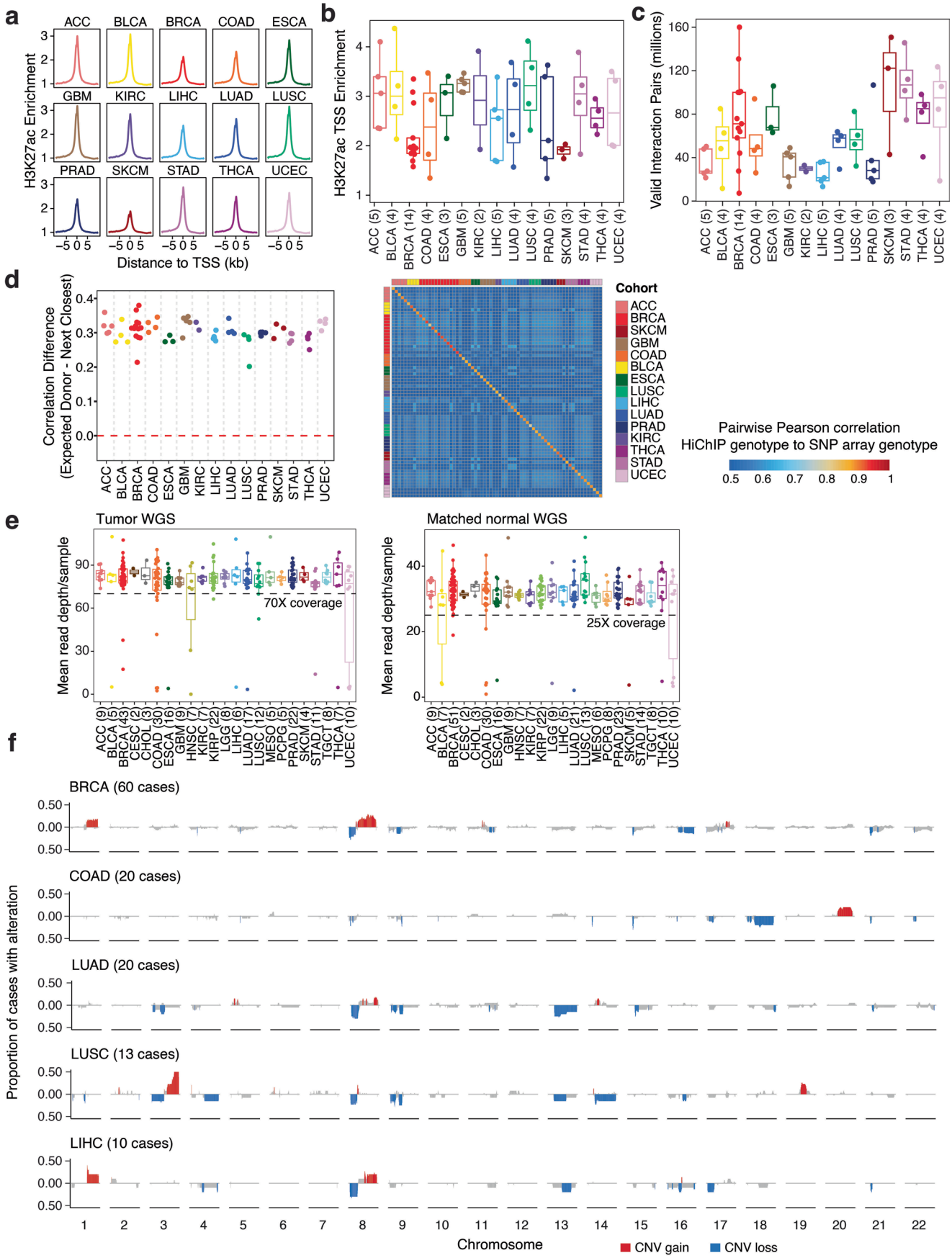

Extended Data Fig. 1 | See next page for caption.

https://doi.org/10.1038/s41588-025-02188-0

Extended Data Fig. 1 | Quality control of H3K27ac HiChIP and WGS data. **a**, Enrichment of HiChIP 1D H3K27ac signal at transcription start sites for all samples merged by cancer type. H3K27ac enrichment per base pair at regions ±2000 bp from the transcription start site is normalized to the number of insertions between ±1900–2000 bp from the transcription start site. **b**, Box plot of the transcription start site enrichment values for all samples of each cancer type. Number of samples from different donors listed for each cancer type. Box centerline, median; box limits, upper and lower quartiles; box whiskers, 1.5× interquartile range. **c**, Box plot of the total valid interaction pairs for all samples of each cancer type. Number of samples from different donors listed for each cancer type. Box centerline, median; box limits, upper and lower quartiles; box whiskers, 1.5× interquartile range. **d**, Genotype correlations between HiChIP genotype and SNP array-derived genotype. Correlation with the next closest match is derived from correlating with all other 69 donors profiled by SNP array by TCGA. Samples that match their expected donor better than all other donors have a correlation difference value above zero (red line, left). Heatmap showing the pairwise Pearson correlation between HiChIP genotype and SNP array genotype, with high correlation along the diagonal indicating HiChIP sample genotypes are most highly correlated with the expected donor genotype based on SNP array (right). **e**, Box plot of the mean read depth per sample for tumor WGS and matched normal WGS. Dashed lines indicate targeted coverage of 70× for tumor WGS and 25× for matched normal WGS. Number of samples from different donors listed for each cancer type. Box centerline, median; box limits, upper and lower quartiles; box whiskers, 1.5× interquartile range. **f**, Genome-wide frequencies of copy-number alterations (CNVs) identified by WGS quantified as proportion of cases with CNV gain ($\log_2$(CNV) > 1) or CNV loss ($\log_2$(CNV) < −1) in 1 Mb genomic windows. Identified CNV alterations are consistent with prior findings, such as chromosome 8q gain in BRCA and LIHC[86–88] and chromosome 3q gain in LUSC [89,90].

https://doi.org/10.1038/s41588-025-02188-0

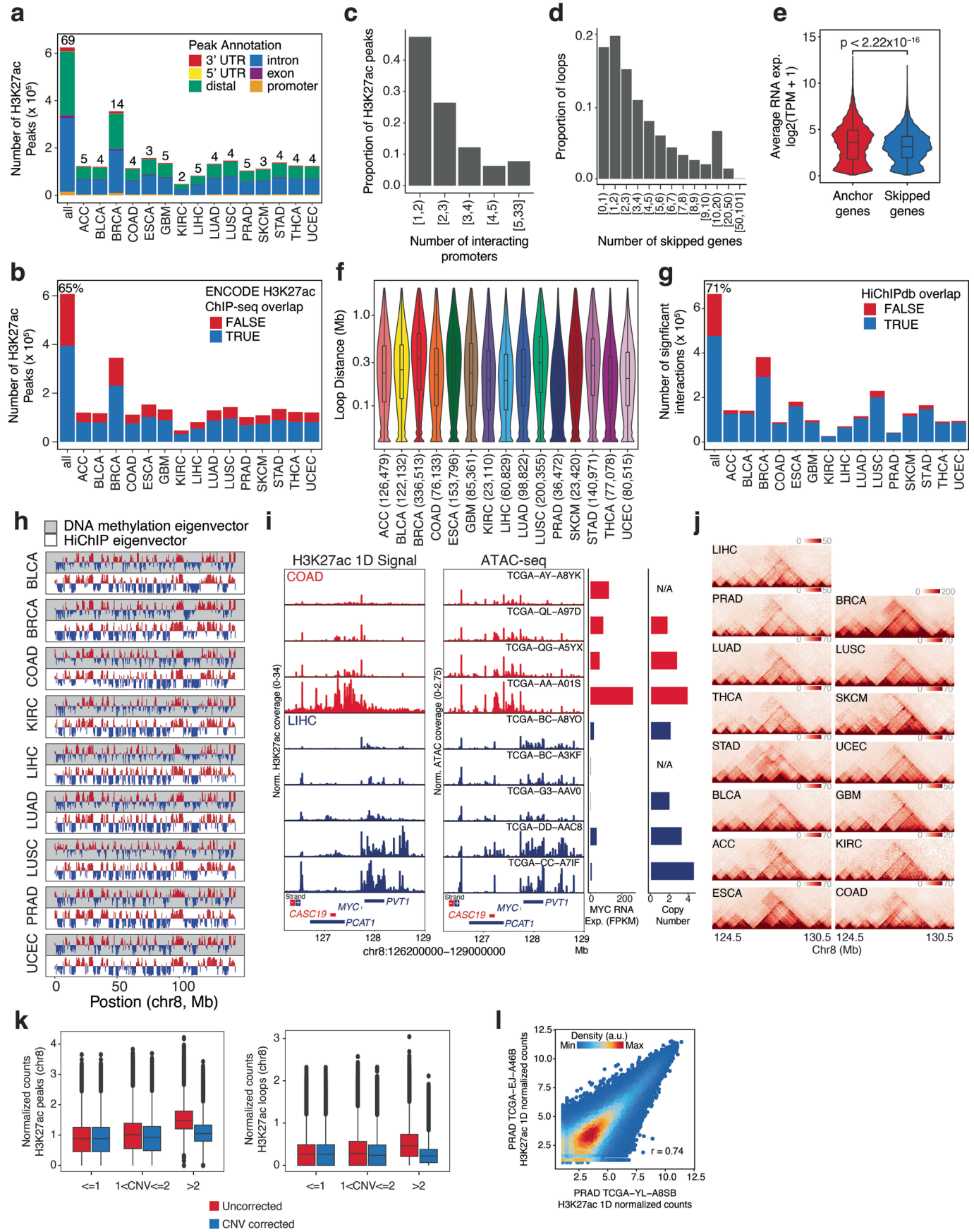

Extended Data Fig. 2 | See next page for caption.

https://doi.org/10.1038/s41588-025-02188-0

Extended Data Fig. 2 | Comparison of HiChIP data with prior epigenomic profiling. a, Stacked bar plot of unique H3K27ac 1D peaks by cancer type colored by peak classification. N = number of samples per cancer type. **b**, Stacked bar plot of unique H3K27ac 1D peaks by cancer type colored by overlap with ENCODE H3K27ac ChIP–seq peaks (Supplementary Table 8). **c**, Bar plot of interacting promoters linked to H3K27ac peaks. **d**, Bar plot of genes skipped by HiChIP loops. **e**, Violin with box plots of the average RNA expression of genes at loop anchors (n = 256,888 gene–loop pairs) and skipped genes between loop anchors (n = 218,050 gene–loop pairs). *P* value determined by two-sided Wilcoxon rank-sum test and not adjusted for multiple comparisons. Box centerline, median; box limits, upper and lower quartiles; box whiskers, 1.5× interquartile range. **f**, Violin with box plot of loop distances by cancer type. N = number of loops detected for each cancer type. Box plot components as in (**e**). **g**, Stacked bar plot of unique significant interactions identified by H3K27ac HiChIP by cancer type and colored by overlap with previously identified loops in HiChIPdb[25]. **h**, Comparison of the first eigenvector of the DNA methylation correlation matrix[26] with the H3K27ac HiChIP eigenvector by cancer type. **i**, Comparison of H3K27ac 1D signal enrichment and bulk ATAC–seq[12] for individual COAD and LIHC samples at the *MYC* locus (left). Bar plot of *MYC* RNA expression and copy number from WGS (right). **j**, KR-normalized H3K27ac HiChIP contact matrix at the *MYC* locus at 50 kb resolution for all samples merged by cancer type. **k**, Box plots of H3K27ac peak (left) and loop (right) signal before and after copy-number normalization for peaks or loops with relative copy number ≤1 (n = 1,684,034 sample-peak pairs and n = 1,051,956 sample–loop pairs), 1 < CN ≤ 2 (n = 2,384,070 sample-peak pairs and n = 978,152 sample–loop pairs), or >2 (n = 166,180 sample-peak pairs and n = 543,760 sample–loop pairs). Box plot components as in (**e**). **l**, Scatter plot of H3K27ac 1D signal enrichment in the union peak set in two PRAD samples. Each dot represents an individual peak.

https://doi.org/10.1038/s41588-025-02188-0

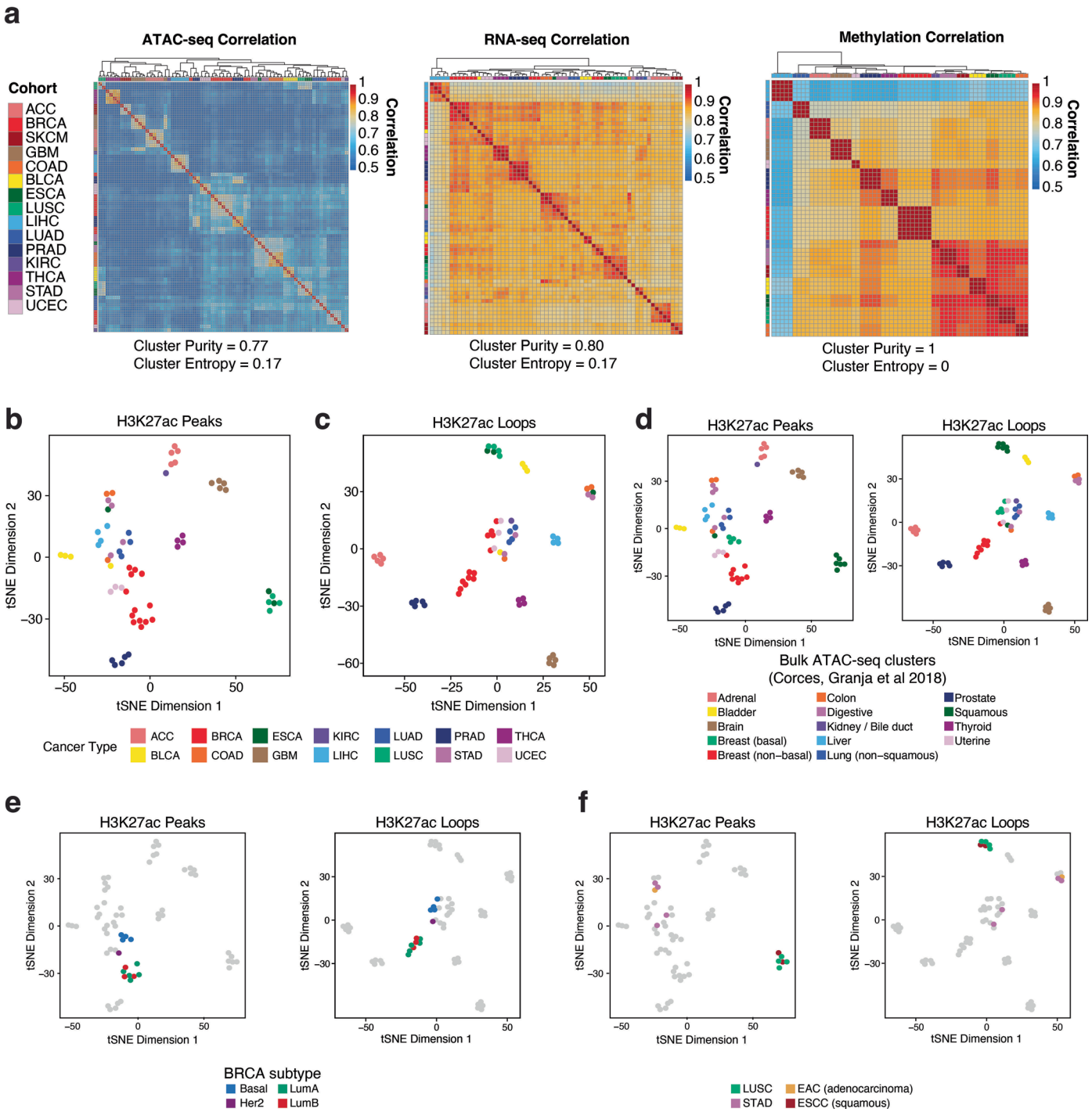

Extended Data Fig. 3 | Unsupervised clustering of H3K27ac peaks and HiChIP interactions. a, Heatmap showing the unsupervised clustering of ATAC−seq, RNA-seq and DNA methylation array. Heatmap colored by Pearson correlation coefficients. Cluster purity quantifies the degree that samples of the same cancer type cluster together with higher values indicating better clustering performance, while for cluster entropy lower values indicate better clustering performance. **b**, Unsupervised t-SNE on the top 15 principal components for the top 10,000 variable H3K27ac peaks in the union peak set across all cancer types. Each dot represents a unique sample colored by cancer type. **c**, Unsupervised t-SNE on the top 10 principal components for the top 10,000 variable H3K27ac HiChIP loops in the union loop set across all cancer types. Each dot represents a unique sample colored by cancer type. **d**, t-SNE colored by bulk ATAC−seq cluster annotations from ref. 12. **e**, t-SNE colored by BRCA subtype[91]. **f**, t-SNE colored by ESCA subtype[33].

https://doi.org/10.1038/s41588-025-02188-0

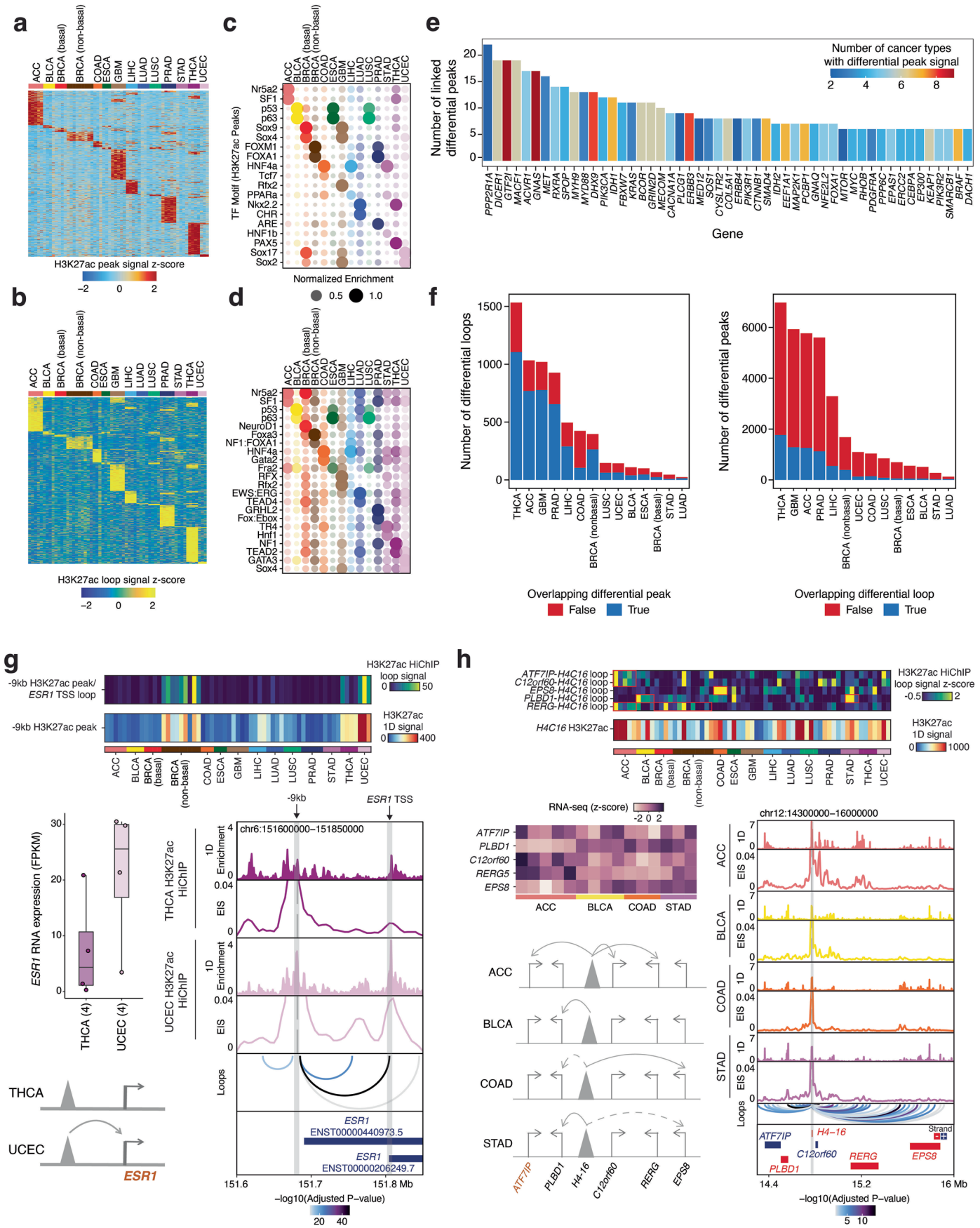

Extended Data Fig. 4 | See next page for caption.

https://doi.org/10.1038/s41588-025-02188-0

Extended Data Fig. 4 | Cancer-type-specific H3K27ac peaks and HiChIP interactions. a, Heatmap of H3K27ac enrichment at cancer-type-specific peaks (n = 28,716). **b**, Heatmap of HiChIP contact enrichment at cancer-type-specific loops (n = 5,073). **c**, TF motif enrichment in cancer-type-specific H3K27ac peaks. **d**, TF motif enrichment in cancer-type-specific loops. **e**, Bar plot of linked differential peaks for oncogenes with >5 differential peaks, colored by number of cancer types with differential peaks. **f**, Stacked bar plot of differential loops colored by overlap with differential peaks for each cancer type (left). All differential loops overlap at least one H3K27ac peak. Stacked bar plot of differential peaks colored by overlap with differential loops for each cancer type (right). Only differential peaks overlapping any identified loops were considered (27,166/28,716 differential peaks). **g**, H3K27ac HiChIP signal z scores across samples for the enhancer–promoter (E–P) interaction between *ESR1* promoter and −9 kb H3K27ac peak (top of top panel). H3K27ac 1D signal z scores across samples for −9 kb H3K27ac peak (top of bottom panel). Box plot of *ESR1* RNA expression (n = number of samples from different donors) and schematic showing the differential E–P interaction (bottom left). Box centerline, median; box limits, upper and lower quartiles; box whiskers, 1.5× interquartile range. Tracks visualize HiChIP 1D H3K27ac enrichment, interaction profiles of the −9 kb enhancer and significant loop interactions colored by adjusted *P* value (bottom right). *P* values were calculated using a two-sided binomial test and corrected using the Benjamini–Hochberg procedure. Two alternative TSS for *ESR1* are annotated; the enhancer is -9kb from the ENST00000440973.5 TSS and looping interactions are analyzed for the ENST00000206249.7 TSS. **h**, H3K27ac HiChIP signal z score across patients for E–P interactions between *ATF7IP*, *PLBD1*, *C12orf60*, *RERG* and *EPS8* promoters and H3K27ac peak at the *H4-16* locus (top of top panel). H3K27ac 1D signal z score across patients for the *H4-16* H3K27ac peak (top of bottom panel). Heatmap of *ATF7IP*, *PLBD1*, *C12orf60*, *RERG* and *EPS8* RNA expression and schematic showing the differential E–P interactions (bottom left). Tracks visualize HiChIP 1D H3K27ac enrichment, interaction profiles of the *H4-16* H3K27ac peak and significant loop interactions colored by adjusted *P* value (bottom right). *P* values were calculated using a two-sided binomial test and corrected using the Benjamini–Hochberg procedure.

https://doi.org/10.1038/s41588-025-02188-0

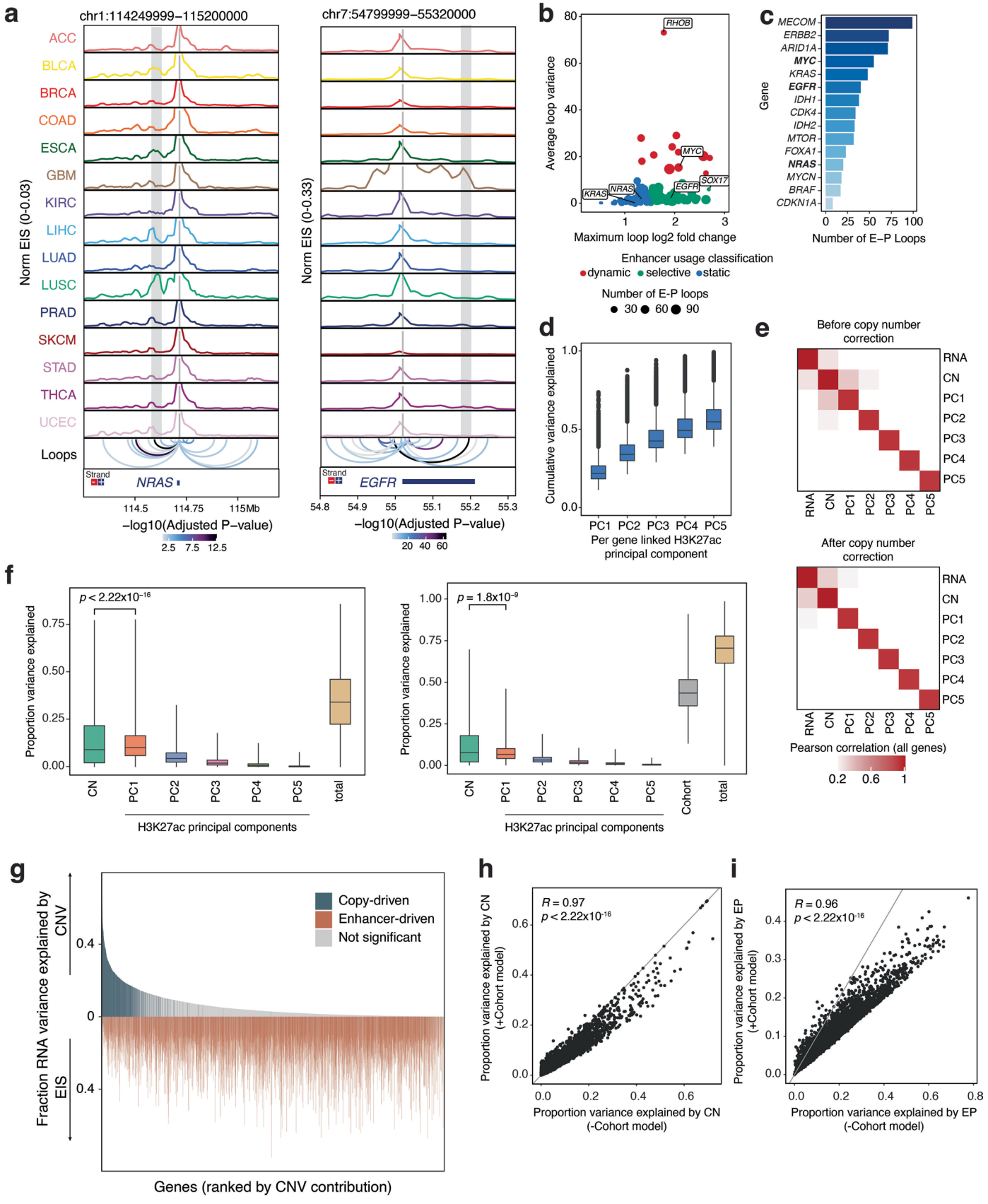

Extended Data Fig. 5 | See next page for caption.

https://doi.org/10.1038/s41588-025-02188-0

Extended Data Fig. 5 | Modeling variance in RNA expression explained by copy number or enhancer activity. a, H3K27ac HiChIP interaction profiles for *NRAS* and *EGFR* for all samples merged by cancer type (right). Significant loop interactions colored by adjusted *P* value shown below. *P* values were calculated using a two-sided binomial test and corrected using the Benjamini–Hochberg procedure. **b**, Scatter plot of average loop variance per oncogene between cancer types versus maximum $\log_2$(fold change) colored by oncogene classification. **c**, Bar plot of unique enhancer–promoter loops for indicated oncogenes. **d**, Box plot of cumulative variance explained by top 5 principal components (PCs) of H3K27ac signal. Each point represents a gene (n = 11,324 genes with linked H3K27ac peaks for each PC). Box centerline, median; box limits, upper and lower quartiles; box whiskers, 1.5× interquartile range. **e**, Heatmap of average Pearson correlation between RNA expression, CNV and top 5 H3K27ac PCs of for all genes (n = 12,570) before and after copy-number regression. **f**, Box plot of variance explained per gene by CNV, top 5 H3K27ac PCs and all variables (left). Box plot of variance explained per gene by CNV, top 5 H3K27ac PCs, cancer type and all variables (right). *P* value determined by two-sided Wilcoxon rank-sum test and not adjusted for multiple comparisons. Box plot components as in (**d**). **g**, All genes with variance in RNA expression >1 (n = 5,985) ranked by fraction of RNA variance explained by CNV across cancer samples, modeled without including cancer type as a variable. Each column is a gene. Genes highlighted on top are significantly (adjusted *P* value < 0.05) explained by CNV (dark blue), while genes highlighted on the bottom are significantly (adjusted *P* value < 0.05) explained by E–P signal (orange). *P* values were calculated using a two-sided t test and corrected using the Benjamini–Hochberg procedure. **h**, Scatter plot of proportion variance explained by copy number with and without including cancer type in regression analysis. *P* value determined by two-sided t test and not adjusted for multiple comparisons. **i**, Scatter plot of proportion variance explained by H3K27ac signal with and without including cancer type in regression analysis. *P* value determined by two-sided t test and not adjusted for multiple comparisons.

https://doi.org/10.1038/s41588-025-02188-0

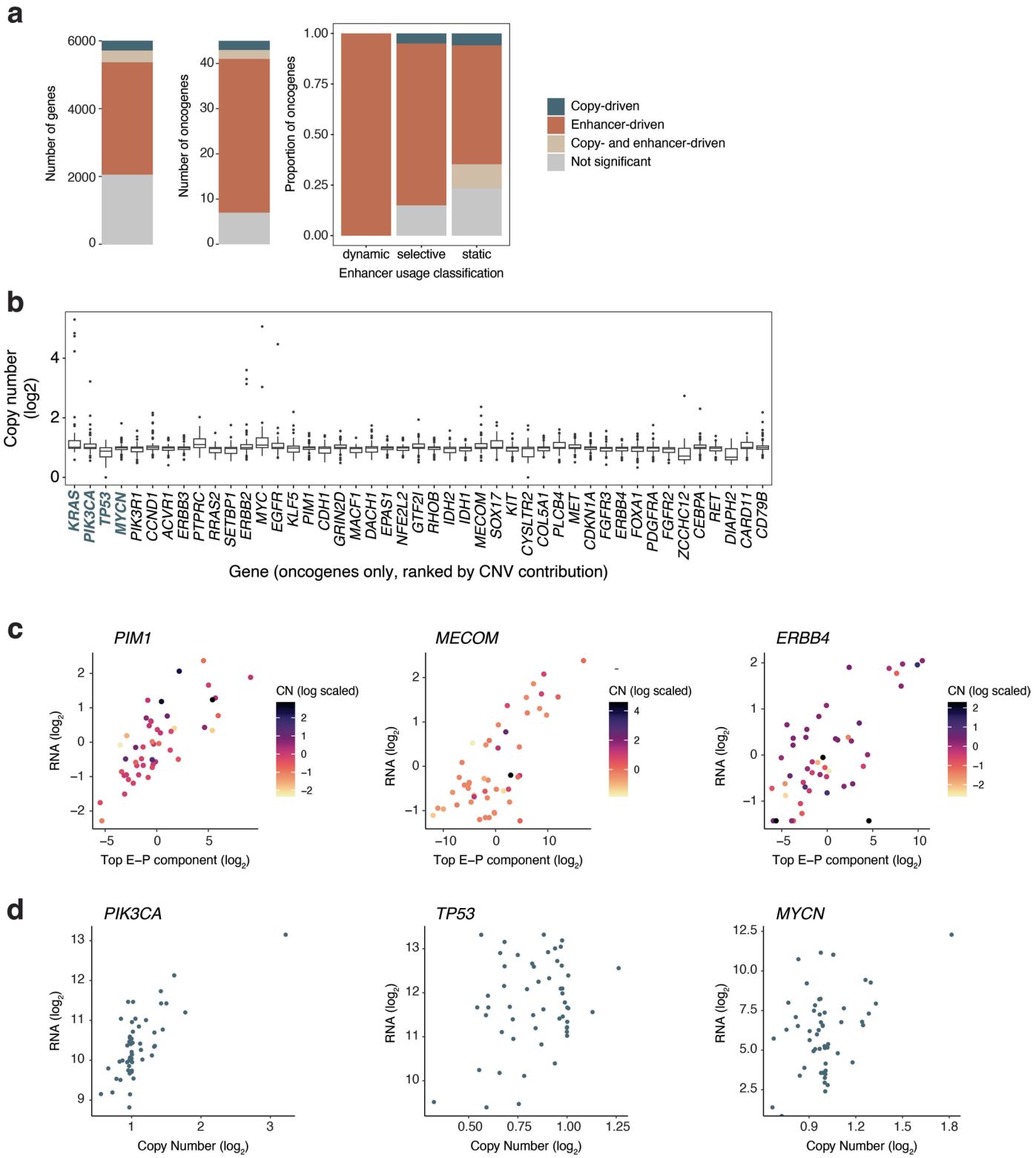

Extended Data Fig. 6 | Copy-driven and enhancer-driven gene classification. **a**, Stacked bar plot of gene classification based on whether variance in RNA expression is significantly explained by DNA copy number, enhancer activity, both or neither based on multiple linear regression analysis for all genes (left), oncogenes (middle) or oncogenes grouped by enhancer usage classification (right). Genes with variance in RNA expression >1 included in modeling analysis (n = 5,985 total genes and n = 45 oncogenes). **b**, Box plot of copy-number distribution for all oncogenes, ranked by CNV contribution in regression analysis for all samples included in analysis (n = 62). Box centerline, median; box limits, upper and lower quartiles; box whiskers, 1.5× interquartile range. **c**, Scatter plot of the relationship between top E–P component and RNA expression for enhancer-driven genes *PIM1*, *MECOM* and *ERBB4*. **d**, Scatter plot of the relationship between DNA copy number and RNA expression for copy-driven genes *PIK3CA*, *TP53* and *MYCN*.

https://doi.org/10.1038/s41588-025-02188-0

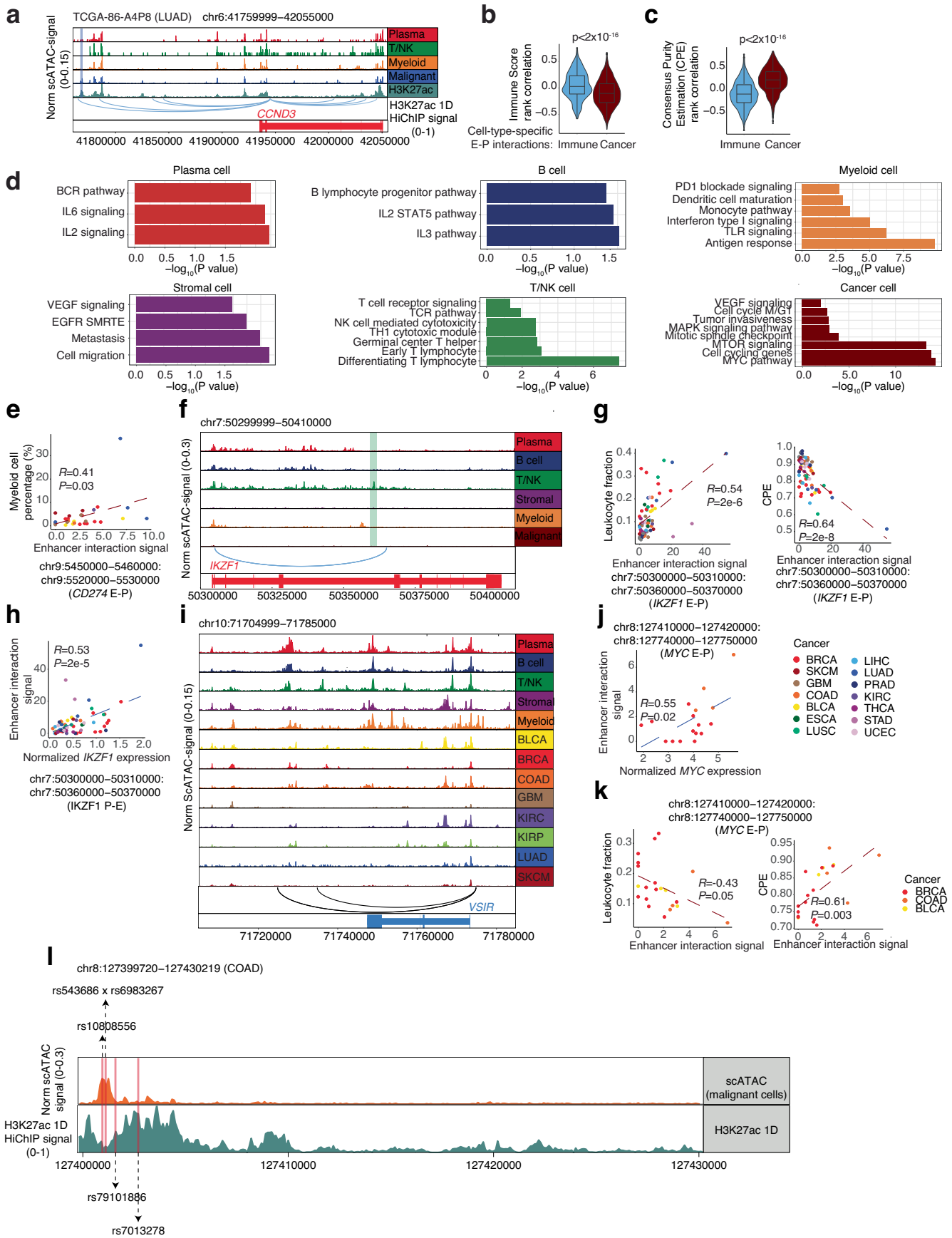

Extended Data Fig. 7 | See next page for caption.

https://doi.org/10.1038/s41588-025-02188-0

Extended Data Fig. 7 | Validation of HiChIP deconvolution framework in tumor microenvironment. a, Signal tracks at the *CCND3* locus. scATAC–seq track shows chromatin accessibility in TCGA-86-A4P8 cells (top), H3K27ac HiChIP track shows bulk H3K27ac signal (middle) and interaction track indicates promoter-associated loops. Shaded region marks a cancer-cell-specific H3K27ac peak. **b**, Violin and box plot showing differences in ImmuneScore correlation coefficients between immune cell-specific (n = 1,029) and cancer-cell-specific (n = 1,551) enhancer–promoter (E–P) interactions. *P* value was calculated using a two-sided Wilcoxon rank-sum test. **c**, Violin and box plot comparing correlation with tumor purity (CPE score) between immune- and cancer-cell-specific E–P interactions. *P* value calculated using a two-sided Wilcoxon rank-sum test. In (**b**,**c**), box centerline denotes median; box limits, upper and lower quartiles; whiskers, 1.5× interquartile range. **d**, Bar plot showing Gene Ontology enrichment of genes regulated by cell-type-specific E–P interactions. *P* values were determined using two-sided Fisher's exact test. **e**, Scatter plot showing correlation between E–P interaction strength and myeloid cell fraction. Correlation coefficient calculated using Pearson correlation; *P* value by two-sided t test. **f**, Signal tracks at the *IKZF1* locus showing merged scATAC–seq signal across eight cancer types (top) and H3K27ac HiChIP interactions (bottom). Shaded region indicates a T/NK cell-specific H3K27ac peak. **g**, Scatter plots showing correlation between *IKZF1* E–P interaction and leukocyte fraction (left) or CPE tumor purity score (right), with Pearson correlation coefficients and *P* values from two-sided t-tests. **h**, Scatter plot showing correlation between *IKZF1* E–P interaction and *IKZF1* RNA expression. Correlation was calculated using Pearson correlation; *P* value by a two-sided t test. **i**, Signal tracks at the *VSIR* locus showing scATAC–seq signal in noncancer and cancer cells across eight cancer types (top) and promoter-associated interactions (bottom). **j**, Scatter plot showing correlation between *MYC* E–P interaction and *MYC* RNA expression, with Pearson correlation coefficient and *P* value from two-sided t test. **k**, Scatter plots showing correlation between *MYC* E–P interaction and leukocyte fraction (left) or CPE tumor purity score (right), with Pearson correlation coefficients and two-sided t test *P* values. **l**, Signal tracks showing scATAC–seq and H3K27ac HiChIP signal at a *MYC* enhancer in COAD, with shaded regions indicating known COAD risk-associated SNPs.

https://doi.org/10.1038/s41588-025-02188-0

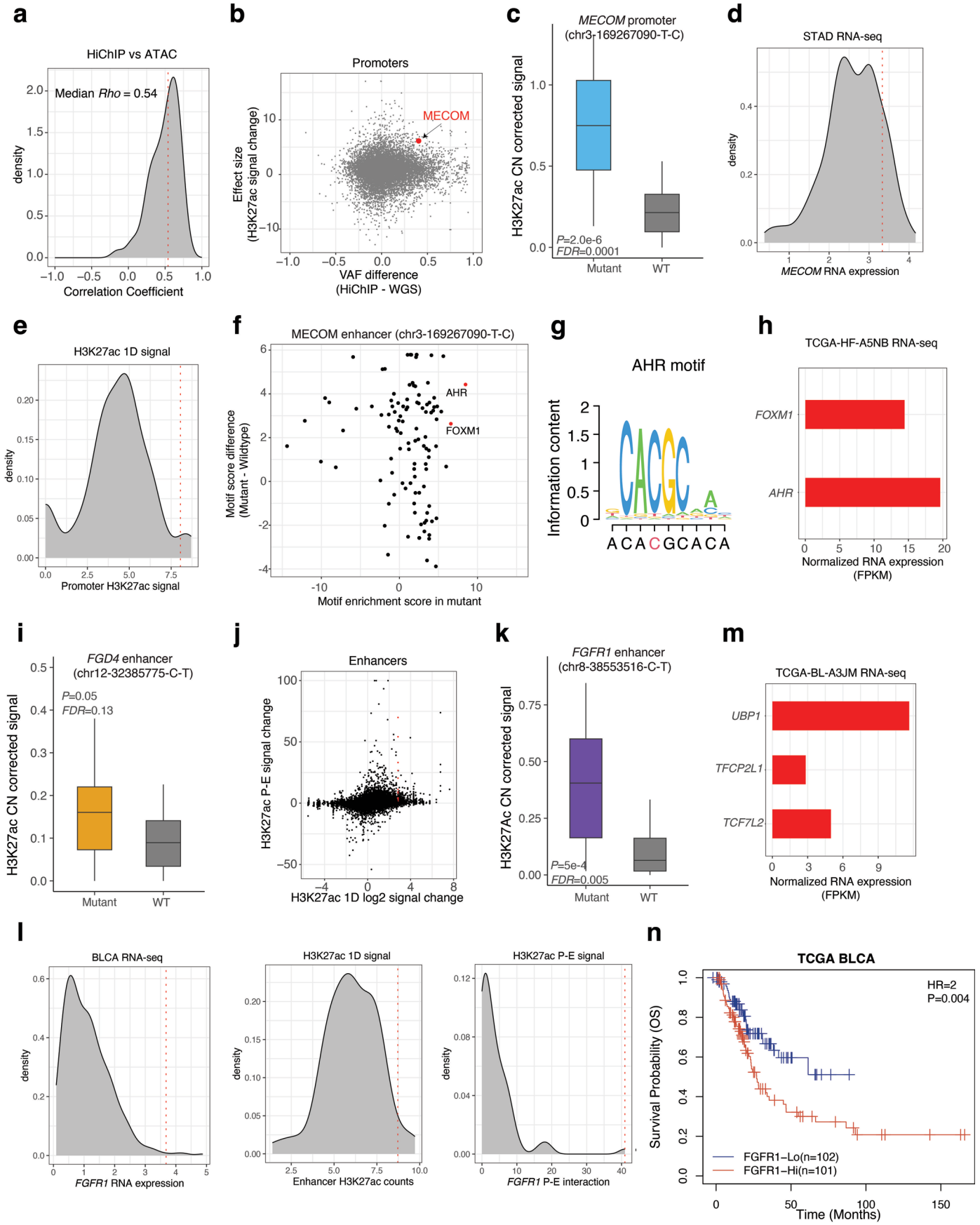

Extended Data Fig. 8 | See next page for caption.

https://doi.org/10.1038/s41588-025-02188-0

Extended Data Fig. 8 | Validation of noncoding mutation-associated H3K27ac signal change. a, Density plot showing distribution of correlation coefficients between mutant allele frequencies derived from H3K27ac HiChIP and ATAC data. **b**, Dot plot showing relationship between promoter-associated HiChIP and WGS allele frequency differences and effect size (*T* score) of corresponding H3K27ac signal changes between mutant and wild-type patients. *T* score was calculated using a two-sided t test. **c**, Box plot showing H3K27ac signal differences in the chr3:169267090-T>C region (±1 kb) between mutant (n = 20 bins from one sample) and wild-type patients (n = 60 bins from three samples). *P* value calculated by two-sided t test and adjusted using Benjamini–Hochberg procedure. Box centerline, median; box limits, upper and lower quartiles; whiskers, 1.5× interquartile range. **d**, Density plot showing distribution of *MECOM* expression in stomach cancer RNA-seq cohort; mutant patient labeled by a red dashed line. **e**, Density plot showing distribution of H3K27ac signal at the *MECOM* promoter in the TCGA HiChIP cohort; mutant patient labeled in red dashed line. **f**, Dot plot showing association between mutant-involved motif enrichment changes at chr3:169267090-T>C and motif enrichment scores. **g**, Motif sequence plot showing overlap between the mutated sequence and the enriched AHR motif. **h**, Bar plot showing RNA expression of enriched transcription factors *FOXM1* and *AHR* in the TCGA-HF-A5NB RNA-seq dataset. **i**, Box plot showing H3K27ac signal difference in the chr12: 32385775-C>T region (±1 kb) between mutant and wild-type patients.
P value calculated by two-sided t test and corrected using Benjamini–Hochberg method. **j**, Volcano plot showing association between enhancer mutations and changes in enhancer activity and enhancer–promoter interactions. **k**, Box plot showing H3K27ac signal difference in the chr8: 38553516-C>T region (±1 kb) between mutant and wild-type patients. Statistical testing as in (**i**). **l**, Density plots showing distribution of *FGFR1* expression, enhancer H3K27ac signal, and enhancer–promoter interactions in the TCGA cohort, with mutant patient values marked by red dashed lines. **m**, Bar plot showing expression of enriched transcription factors *UBP1*, *TFCP2L1* and *TCF7L2* in TCGA-BL-A3JM RNA-seq data. **n**, Kaplan–Meier plot showing prognostic value of *FGFR1* expression; patients stratified into high and low groups based on top and bottom 25% percentiles. *P* value by log-rank test.

https://doi.org/10.1038/s41588-025-02188-0

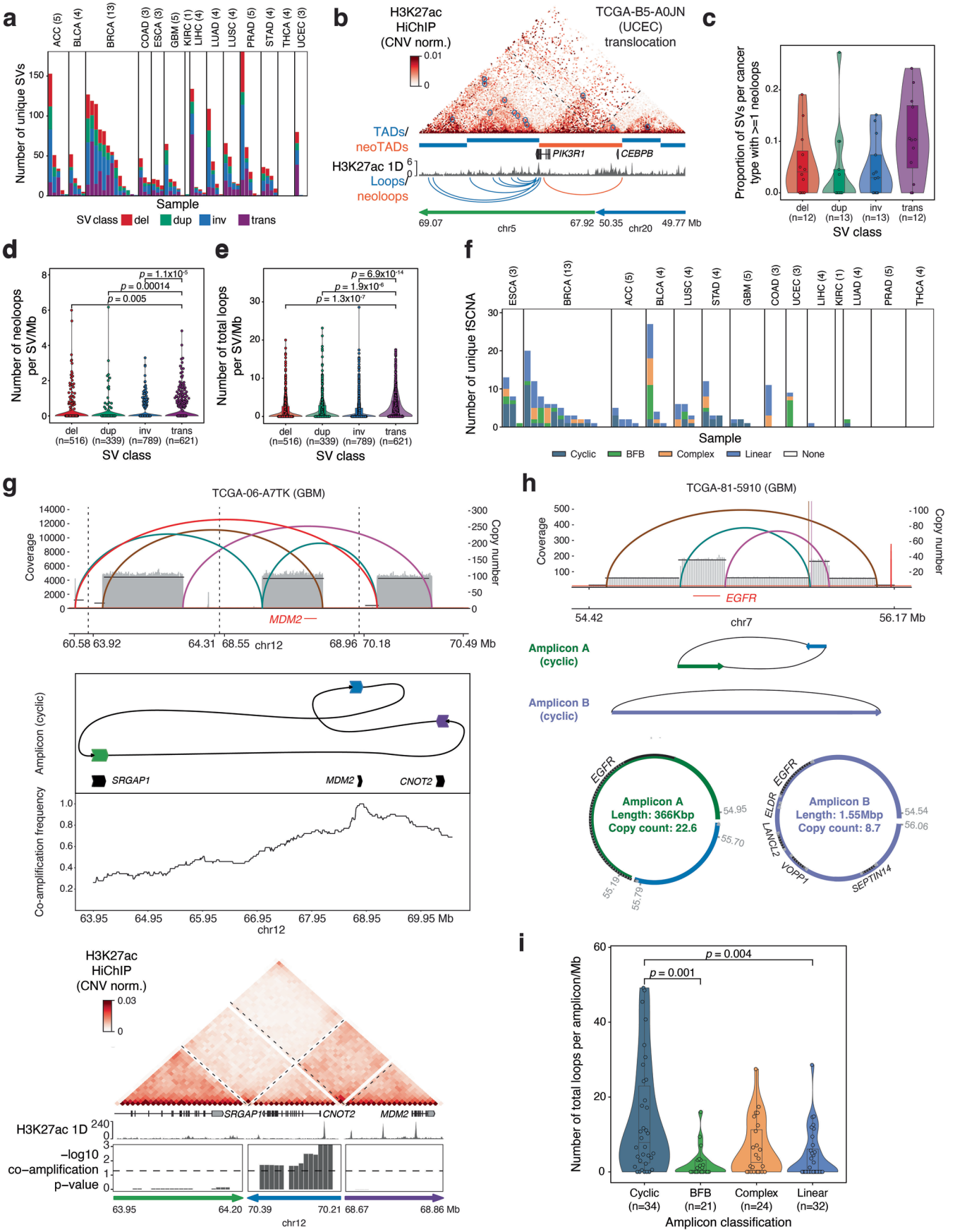

Extended Data Fig. 9 | See next page for caption.

https://doi.org/10.1038/s41588-025-02188-0

Extended Data Fig. 9 | Structural rearrangements affecting enhancer rewiring. **a**, Distribution of simple SVs detected across individual samples (del = deletion, dup = duplication, inv = inversion, trans = translocation). **b**, Copy-number-normalized HiChIP contact matrix for *PIK3R1* translocation with tracks visualizing TADs/neoTADs, H3K27ac 1D signal enrichment and loops/neoloops. **c**, Box and violin plots of the proportion of SVs per cancer type with ≥1 neoloop detected (n = number of cancer types). SVs that overlap with focal amplification breakpoints identified by AmpliconArchitect are excluded in **c**–**e**. Box centerline, median; box limits, upper and lower quartiles; box whiskers, 1.5× interquartile range. **d**, Box and violin plots of the number of neoloops per SV per megabase (n = number of SVs). Box centerline, median; box limits, upper and lower quartiles; box whiskers, 1.5× interquartile range. **e**, Box and violin plots of the number of total loops per SV per megabase (n = number of SVs). Box centerline, median; box limits, upper and lower quartiles; box whiskers, 1.5× interquartile range. **f**, Distribution of cyclic, BFB, complex, linear focal somatic copy-number amplifications (fSCNA) detected across individual samples. **g**, Cyclic structural rearrangement predicted by AmpliconArchitect affecting the *MDM2* locus (top). Amplicon structure and co-amplification frequency across all TCGA WGS samples (middle). Tracks visualizing H3K27ac 1D signal enrichment and significance of co-amplification with copy-number normalized HiChIP matrix below (bottom). **h**, Cyclic structural rearrangement predicted by AmpliconArchitect affecting the *EGFR* locus (top). Schematic of predicted ecDNA structures (bottom). **i**, Number of loops within cyclic, BFB, complex, linear amplifications identified by NeoLoopFinder. Loop counts are quantified for each focal amplification, normalized by the size of the focal amplification. *P* values were calculated using a two-sided Wilcoxon rank-sum test and adjusted using the Benjamini–Hochberg procedure. Box centerline, median; box limits, upper and lower quartiles; box whiskers, 1.5× interquartile range.

nature portfolio

Corresponding author(s): Howard Y. Chang, William J. Greenleaf

Last updated by author(s): Feb 13, 2025

Reporting Summary

Nature Portfolio wishes to improve the reproducibility of the work that we publish. This form provides structure for consistency and transparency in reporting. For further information on Nature Portfolio policies, see our Editorial Policies and the Editorial Policy Checklist.

Statistics

For all statistical analyses, confirm that the following items are present in the figure legend, table legend, main text, or Methods section.

n/a	Confirmed
☐	☒ The exact sample size (*n*) for each experimental group/condition, given as a discrete number and unit of measurement
☐	☒ A statement on whether measurements were taken from distinct samples or whether the same sample was measured repeatedly
☐	☒ The statistical test(s) used AND whether they are one- or two-sided *Only common tests should be described solely by name; describe more complex techniques in the Methods section.*
☒	☐ A description of all covariates tested
☐	☒ A description of any assumptions or corrections, such as tests of normality and adjustment for multiple comparisons
☐	☒ A full description of the statistical parameters including central tendency (e.g. means) or other basic estimates (e.g. regression coefficient) AND variation (e.g. standard deviation) or associated estimates of uncertainty (e.g. confidence intervals)
☐	☒ For null hypothesis testing, the test statistic (e.g. *F*, *t*, *r*) with confidence intervals, effect sizes, degrees of freedom and *P* value noted *Give P values as exact values whenever suitable.*
☒	☐ For Bayesian analysis, information on the choice of priors and Markov chain Monte Carlo settings
☒	☐ For hierarchical and complex designs, identification of the appropriate level for tests and full reporting of outcomes
☐	☒ Estimates of effect sizes (e.g. Cohen's *d*, Pearson's *r*), indicating how they were calculated

Our web collection on statistics for biologists contains articles on many of the points above.

Software and code

Policy information about availability of computer code

Data collection

HiChIP data were processed as described previously. In brief, paired-end reads were aligned to the hg38 genome using the HiC-Pro pipeline (v.2.11.0). Default settings were used to remove duplicate reads, assign reads to MboI restriction fragments, filter for valid interactions and generate binned interaction matrices.

WGS sequencing reads were aligned to the hg38 genome using bwa-mem (version 0.7.15).

Data analysis

HiChIP data analysis
FitHiChIP (v.8.0) were used to identify loops. Dangling end, self-circularized, and re-ligation read pairs were merged with valid read pairs to create a one-dimensional H3K37ac signal bed file, corresponding to H3K27ac ChIP-seq-like signal which was used for peak calling and 1D signal quantification using standard ChIP-seq analysis tools including MACS2 (v2.2.7.1). FitHiChIP was used to identify 'peak-to-all' interactions at 10-kb resolution using peaks called from the one-dimensional HiChIP data using MACS2. A lower distance threshold of 20kb was used. Bias correction was performed using coverage specific bias. HiChIP loop calling was performed at 10kb resolution to balance resolution for identifying relevant enhancer-promoter interactions with sensitivity in loop calling which improves at lower resolutions. Per-sample loop calling generated on average 112,081 unique significant interactions per sample, ranging from 580 to 436,780. Filtered read pairs from the HiC-Pro pipeline were converted into .hic format files for visualization and normalization.

WGS analysis
WGS variants were called using the GDC/Sanger Whole Genome Sequencing Variant Calling pipeline (https://docs.gdc.cancer.gov/Data/Bioinformatics_Pipelines/DNA_Seq_Variant_Calling_Pipeline/#whole-genome-sequencing-variant-calling). Briefly, SNV calls were generated with CaVEMan (version 1.15.5), small insertions/deletions identified using Pindel (version 2.0), structural variants identified using BRASS (https://github.com/cancerit/BRASS, version 6.2.1), and somatic copy number alterations identified using AscatNGS (version 4.2.1). WGS read

depth statistics were generated using mosdepth (version 0.3.1). We performed quality control on copy number calls (CNVs) generated using ASCAT pipeline by comparing with manually-reviewed calls from running ABSOLUTE (version 1.0.6) pipeline on SNP array data.

HiChIP data QC - Transcription start site enrichment
Enrichment of H3K27ac HiChIP signal at transcription start sites (TSSs) was used to quantify H3K27ac ChIP enrichment quality, similar to ATAC-seq quality control (Corces et al., 2018). First, allValidPairs generated by HiC-Pro were read into a GenomicRanges object in R. Pairs separated by more than 10 kb were excluded. TSSs were obtained from TxDb.Hsapiens.UCSC.hg38.knownGene (version 3.10.0) and extended 2000 bp in each direction and overlapped with fragments (both ends of a valid pair) using GenomicRange's findOverlaps. Next, the distance between the fragments and the strand-corrected TSS was calculated and the number of fragments occurring in each single-base bin was summed. To normalize this value to the local background, the enrichment at each position +/- 2000 bp from the TSS was normalized to the mean of the enrichment at positions +/-1900-2000 bp from the TSS. The final TSS enrichment reported was the maximum enrichment value within +/- 50 bp of the TSS after smoothing with a rolling mean every 51 bp.

HiChIP data QC - genotype correlation with TCGA SNP array data
In order to validate the authenticity of HiChIP data attributed to specific TCGA donors and their corresponding tissues, we conducted genotyping analyses. Our approach involved comparing our HiChIP data (N=69 individual sequencing experiments) with SNP calls extracted from TCGA SNP array data utilizing the Affymetrix SNP 6.0 array (N=11,127 TCGA donors). This SNP array data, having been previously generated by TCGA, serves as our benchmark for validation. To achieve this, we overlapped genomic locations probed by the Affymetrix SNP 6.0 array (932,148 hg38-mappable probes) with peak regions identified in all HiChIP samples. The genotypic information for each HiChIP BAM file was then collected at 124,773 SNP locations and converted into a birdseed-style format. Notably, a minimum read depth of 6 was set as a prerequisite for SNP calls. In the HiChIP data, positions were labeled as homozygous if reads mapped exclusively to either the A or B allele, resulting in a birdseed call of 0 or 2. Conversely, positions were categorized as heterozygous if the absolute difference between allele A and allele B counts was less than 50% of the total depth, leading to a birdseed value of 1. Positions exhibiting substantial allelic imbalance were classified as homozygous due to excessive disparity, with a birdseed value of 0 or 2. Each birdseed-style HiChIP genotyping list was correlated with TCGA Affymetrix SNP 6.0 array data (11,127 individual donors). Pearson correlations were computed solely for HiChIP BAM files at genomic locations with a viable SNP call in the HiChIP data (locations with read depth exceeding 6). Samples were considered successful if their correlation with the expected biological donor surpassed the correlation with all other 11,126 TCGA donors, affirming concordance between HiChIP data and Affymetrix SNP 6.0 array data, and thereby validating their shared origin.

Interaction and H3K27ac peak annotation
We annotated significant HiChIP interactions identified by FitHiChIP based on overlap with gene promoters and/or enhancers. First we intersected FitHiChIP loop anchors with gene promoters obtained from TxDb.Hsapiens.UCSC.hg38.knownGene (version 3.10.0) and extended by +/- 1kb. Anchors that did not overlap with a gene promoter were then intersected with the union H3K27ac peak set to identify anchors that overlap with putative enhancers. HiChIP interactions were then annotated as either E-P: enhancer-promoter, E-E: enhancer-enhancer, P-P: promoter-promoter, E-N: enhancer-neither, P-N: promoter-neither. Merged H3K27ac peaks were annotated using HOMER's annotatePeaks.pl (version 4.11) (Heinz et al., 2010). H3K27ac HiChIP 1D peaks were overlapped with ENCODE H3K27ac ChIP-seq peaks obtained from MACS narrowPeak files from primary tissue samples with accession numbers listed in Supplementary Table 8. Number of interacting gene promoters with H3K27ac peaks and number of genes skipped by loops were determined using GenomicRanges' findOverlaps function (version 1.42.0) with gene promoters obtained from TxDb.Hsapiens.UCSC.hg38.knownGene (version 3.10.0).

Comparison to HiChIPdb loops
10kb resolution FitHiChIP loops from H3K27ac HiChIP experiments were downloaded from HiChIPdb (Zeng et al., 2023). hg19 coordinates were converted to hg38 using the easyLiftOver function from the R package easyLift (https://github.com/caleblareau/easyLift, version 0.2.1). Loop sets were converted to GenomicInteractions format in R (version 1.24.0) and the intersection between HiChIPdb loops and our loop set was determined using GenomicRanges' findOverlaps function (version 1.42.0).

Interaction matrix visualization
2D interaction matrices were visualized using Juicebox (version 1.11.08) or with the plotgardener package in R (version 1.2.10) (Kramer et al., 2022).

Eigenvector calculation and A/B compartment annotation
The eigenvector (first principal component of the Pearson's matrix) for H3K27ac HiChiP observed/expected interaction matrices was obtained from .hic files using juicer_tools eigenvector function (version 1.9.9) at 500 kb resolution with KR normalization. The sign of the eigenvector and A/B compartment annotation was assigned based on correlation with DNA methylation eigenvector and compartment analysis obtained from Additional File 2 of Fortin and Hansen, 2015 (Fortin and Hansen, 2015). A positive eigenvector sign is used to indicate A (open) compartment and negative sign to indicate B (closed) compartment, the opposite of Fortin & Hansen, 2015, and thus the eigenvector sign is flipped relative to the sign in Fortin & Hansen, 2015. For hierarchical clustering in Figure 1f, we used CALDER (Liu et al., 2021) (version 2.0) to obtain sub-compartment calls at 10 kb resolution and performed clustering using vectorized sub-compartment annotations based on the compartment rank annotation returned by CALDER.

H3K27ac 1D signal and virtual 4C visualization
One dimensional H3K27ac enrichment and ATAC-seq signal was visualized following normalization by reads in TSS regions as described in the ArchR package (Granja et al., 2020). ATAC-seq signal tracks were obtained from the GDC publication page (Corces et al., 2018). H3K27ac ChIP-seq signal tracks were obtained from ENCODE (accessions ENCFF905FLR and ENCFF873MWG) (Dunham et al., 2012; Luo et al., 2020). Virtual 4C plots were generated from dumped matrices generated with Juicer Tools (1.9.9). The Juicer Tools tools dump command was used to extract the chromosome of interest from the .hic file. The interaction profile of a 10-kb bin containing the anchor was then plotted in R (v.4.0.3) after normalization by the total number of valid read pairs and smoothing with the rollmean function from the zoo package (v.1.8-9).

Generation of union H3K27ac peak and interaction count matrices
One dimensional H3K27ac peaks called by MACS2 were merged using bedtools merge and peak signal calculated using bedtools coverage using one-dimensional H3K27ac signal bed files (v2.28.0). Significant HiChIP interactions identified by FitHiChIP were merged using FitHiChIP's CombineNearbyInteraction.py and loop signal calculated using pgltools coverage (version 2.2.0) (Greenwald et al., 2017). Raw peak and loop signal was normalized using DESeq2's size factors normalization obtained using counts (dds,normalized=TRUE) (version 1.30.1) (Love et al., 2014). CNV correction was performed for cases with matching WGS data by dividing normalized signal by ploidy-corrected relative CNV values for peaks or loops overlapping with amplified genomic intervals (relative CNV > 1). Peaks or loops that overlapped genomic intervals with CNV equal to zero or no CNV call were converted to NA values for those samples. For CNV correction of 2D loop signal, the relative CNV value of

each loop anchor was determined and the normalized loop signal divided by the product of the CNV values at the two anchors. Seven samples did not have matched WGS data for CNV correction and were excluded from further analysis.

Unsupervised hierarchical clustering, cluster purity calculation, and dimensionality reduction
Eigenvectors for H3K27ac HiChIP interaction matrices for chromosomes 1-22 were obtained from .hic files using juicer_tools eigenvector function (version 1.9.9) at 1 Mb resolution with KR normalization and pairwise Pearson correlations calculated using the cor function in R using "pairwise.complete.obs". Heatmap visualization and hierarchical clustering were performed using the pheatmap function in R (version 1.0.12). Clustering assignments were obtained using the cutree function in R with k equal to the number of unique cancer types. Clustering purity and entropy were calculated using the purity and entropy functions from the NMF package in R (version 0.26) (Gaujoux and Seoighe, 2010).

For 1D H3K27ac and loop signal clustering, pairwise Pearson correlations were calculated using the normalized, copy-number corrected count matrices. Peaks and loops on chrX and chrY and those overlapping hg38 blacklist regions (Amemiya et al., 2019) (https://github.com/Boyle-Lab/Blacklist/blob/master/lists/hg38-blacklist.v2.bed.gz) were excluded from analysis. Correlation analysis was performed on reproducible peaks and loops where at least two samples had a normalized count value >=3. Count matrices were log2 transformed using a prior count of 1 to reduce the contribution of variance from elements with low count values and to avoid taking the log of zero. Visualization, clustering and purity calculations were performed as described above. The same count matrices were used for dimensionality reduction and visualization using t-Distributed Stochastic Neighbor Embedding (t-SNE). Log-transformed counts were scaled using Seurat's ScaleData and element counts were ranked by variance using matrixStats rowVars function. The top 10,000 variable elements were used for principal component analysis (PCA) using Seurat's RunPCA function. The top 15 PCs were used for t-SNE dimensionality reduction using Seurat's RunTSNE with perplexity = 5. Samples were colored by cancer type, bulk ATAC-seq cluster annotation (Corces et al., 2018), BRCA subtype (Sanchez-Vega et al., 2018), and ESCA subtype (Cancer Genome Atlas Research Network et al., 2017).

Identification of differential H3K27ac peaks and HiChIP loops by feature binarization
We executed the identification of 'unique' peaks within the HiChIP data, adhering to a predefined methodology. In essence, we log2-transformed the copy number corrected H3K27ac peak count matrix, categorizing individual cancer types as distinct 'groups'. For each peak within the HiChIP peak set, we computed both intragroup mean and standard deviation values. Subsequently, these groups were ranked based on their respective intragroup mean scores. Through an iterative process, we initiated from the second-lowest-ranked group and gauged whether its mean value surpassed the sum of the maximum intragroup mean and the intragroup standard deviation of the subsequent-lower group. This iterative sequence persisted until a group meeting this particular criterion was identified. This point defined the 'breakpoint'. Groups boasting intragroup means exceeding the breakpoint were labeled '1' for that specific peak, while groups situated below the breakpoint received a '0' designation. Peaks lacking a breakpoint were excluded. This 'binarization' process established all '1s' as being greater than any individual '0', thus capturing peaks unique to multiple groups. Combinations present in three or fewer groups were retained. To address multiple hypothesis testing, we devised a contrast matrix for observed combinations and subjected the log-normalized counts matrix to limma's (v.3.38.3) eBayes test. Subsequently, we extracted false discovery rate (FDR)-adjusted P values from differential testing, preserving peaks with FDR values below 0.01. Employing the same aforementioned methodology, we also determined the 'unique' interactions within the HiChIP data by using the log2-transformed copy number corrected H3K27ac interaction count matrix. For motif enrichment analysis, we transformed the 'unique' peaks of each cancer type into the bed format. However, due to the vast genomic span covered by 'unique' interactions, conducting direct motif enrichment analysis proved challenging. As a solution, we intersected the 'unique' interactions per cancer type with the corresponding H3K27ac peaks. Peaks overlapping both anchors were consolidated into the bedgraph format to facilitate motif enrichment analysis. The findMotifsGenome function from HOMER software (v4.11.1) was employed for this purpose, using the parameter '-size given'.

Enhancer rewiring analysis
Using the normalized and copy number corrected consensus FitHiChIP loops from H3K27ac HiChIP 3D data, we intersected the loop anchor with consensus peaks from H3K27ac 1D data as well as promoters of gene transcripts. Promoters are defined as -2500/+250 bp of each TSS using GENCODE v36. In situations where the peak is involved in a given peak-promoter interaction in one sample but not called as a peak by H3K27ac 1D in that sample, "0" will be assigned to the peak-promoter interaction for that given sample. We also focused on enhancer-promoter interactions by excluding H3K27ac 1D peaks overlapping any promoters when interacting with another promoter. Overall, from consensus loops with 10kb anchors, we identified 894,776 enhancer-promoter interactions.

Modeling of oncogene expression with copy number and enhancer activity
To determine the relative contributions of copy number and enhancer activity to variability in oncogene expression, we integrated H3K27ac peaks and interactions, WGS ploidy-corrected CNV calls and HTSeq counts from RNA-seq data for annotated gene loci. Samples missing from any of these datasets were excluded from this analysis. RNA-seq raw counts were normalized using DESeq2's size factors normalization obtained using counts (dds,normalized=TRUE) (version 1.26.0). Union H3K27ac peaks within 1 Mb away from annotated gene TSSs that were supported by peak-TSS interaction loops in HiChIP were considered. To account for increased HiChIP read counts due to CNV, read counts of these TSS-associated H3K27ac peaks were normalized to ploidy-corrected copy numbers as follows: CNV-normalized peak count = (DESeq2-normalized peak count) / (ploidy-corrected copy number * 2 + 1). To assess the variability in gene expression, we first filtered on expressed genes defined as genes with more than 10 transcripts per million (TPM) in more than three samples in the RNA-seq dataset. We then used multiple linear regression to model the DESeq2-normalized RNA-seq gene expression values using the formula RNA ~ H3K27ac + CN, where RNA is the DESeq2-normalized RNA-seq gene expression value, H3K27ac represents terms of log2-transformed, scaled and centered 1D H3K27ac counts of peaks associated with the given gene, and CN represents the ploidy-corrected copy number of the gene. For genes with which more than five H3K27ac peaks were associated, log2-transformed, scaled and centered 1D H3K27ac counts were reduced to five principal components using the pca function in R with ncomp = 5, center = TRUE, scale = TRUE. For genes with 5 or less linked H3K27ac peaks, individual peak signal was used as input for RNA expression modeling rather than PCs. Relative importance of model predictors for each gene was quantified with the Lindeman, Merenda, and Gold (LMG) method using the calc.relimp function in R with type = "lmg", rela = FALSE. To analyze the relative importance of H3K27ac HiChIP signal and copy number of oncogenes, we curated a list of oncogenes and possible oncogenes based on previous analysis (Bailey et al., 2018). Log2 transformation of count data was performed as log2 (count + 1) unless specified otherwise.

Sample specific scATAC-seq data analysis
The processed scATAC-seq archR object (v1.0.1) with cell type annotation was downloaded from https://www.synapse.org/. For each sample with matched H3K27ac HiChIP data, we regenerated archR object and re-calcuated chromatin accessibility peaks for each cell population through MACS2 (v2.1.1) under default setting.

HiChIP integration with scATAC-seq
29 samples with matched H3K27ac HiChIP and scATAC-seq data. A minimum number of 110 non-cancer cells were required in each sample to ensure the power of scATAC-seq peak signal detection in the tumor microenvironment, which ends up with 16 samples for integration. For each matched sample, we examined the co-occurence of H3K27ac peaks and scATAC-seq peaks in the anchor regions of promoter-enhancer interactions. The cell type specific promoter-enhancer interaction was identified when (1) the promoter region of the regulated gene had both H3K27ac and scATAC-seq peaks, (2) the enhancer region defined by the HiChIP interactions had H3K27ac peaks but was uniquely accessible in a specific cell type. The cell type shared promoter-enhancer interaction was defined when the promoter or enhancer regions had both H3K27ac and scATAC-seq peaks but were not limited to a specific cell type. The ambiguous promoter-enhancer interaction was defined when both promoter and enhancer region cannot map to any scATAC peaks. To generalize our sample-specific analysis to the broader population, we performed a correlation analysis between the promoter-enhancer interaction signal and the corresponding cell fraction in the tumor microenvironment. We obtained these cell fractions from scATAC-seq and estimated leukocyte fractions from RNA-seq data. The Spearman correlation coefficient (Rho) was calculated for each correlation, and we applied cutoff values of Rho ≥ 0.30 and Rho ≥ 0.25 to filter the results. For validation of H3K27ac HiChIP deconvolution in tumor microenvironment, the RNA-seq derived leukocyte fraction estimation, ImmuneScore and tumor purity estimation were downloaded respectively from the original publication for correlation analysis (Aran et al., 2015; Thorsson et al., 2018; Yoshihara et al., 2013).

HiChIP integration with cancer associated SNP sites
Cancer-associated SNP data were retrieved from the database available at https://www.ebi.ac.uk/gwas/. We augmented the SNP list by incorporating SNPs in high Linkage Disequilibrium (LD) with GWAS lead SNPs (LD r2 > 0.8). This LD data was sourced from the haploreg website (http://archive.broadinstitute.org/mammals/haploreg/data/). To identify potential regulatory elements associated with these SNPs, we performed an intersection analysis with enhancer peaks. The enhancer peaks were obtained from malignant cell-specific promoter-enhancer interactions, as determined through our prior HiChIP decomposition analysis. This approach allowed us to pinpoint genomic positions where cancer-associated SNPs coincided with enhancer elements.

Identification of non-coding mutation involved H3K27ac modification
62 samples with matched H3K27ac HiChIP and WGS data. We used the somatic mutation calling from WGS data as the ground truth. The mutation allele frequency of H3K27ac HiChIP data was generated using bcfools. First, the global aligned H3K27ac bam files from the FitHiChIP pipeline were piled up through mpileup function from bctools (v1.17). Then, the derived bcf files were converted into vcf files through call function from bcftools. The allele frequency of each somatic mutation was quantified from the vcf files accordingly. The reads coverage of H3K27ac HiChIP at the somatic mutation site was calculated through multiBamSummary from deeptools. The mutation with at least 30 H3K27ac reads coverage was taken as confident calls. The significance of the mutant allele was estimated using Fisher's Exact Test, followed by Benjamini-Hochberg (BH) method for multiple comparison correction.
The H3K27ac signal change involved in the mutation site was quantified using the 2kb window that centered at the mutation position. The 2kb window was splitted into 20bins with each bin equal to 100 bp. The H3K27ac HiChIP signal was calculated through multiBamSummary from deeptools (v2.0) and normalized by the library size and copy number. For each mutation, we performed T test between mutant samples and wild type samples to quantify the difference of CNV corrected H3K27ac signals. To perform multiple comparison correction, we utilized the Benjamini-Hochberg (BH) method.

Quantification of non-coding mutation involved motif enrichment changes
chromVARmotifs R package (v0.2) was used for collection of human transcription factor binding motifs. motifmatchr R package was used for performing motif enrichment analysis. First, a 21 bp sequence centered at mutation position was derived. Then, matchMotifs function was applied to the 21bp sequences from mutant and wildtype for motif enrichment calculation under parameter out="positions" with a p value cutoff 0.01.

AmpliconArchitect reconstruction of complex structural rearrangements
We collected 120 tumor WGS samples from 16 distinct cancer types and 123 matched normal WGS samples from TCGA, all aligned to GRCh38. We ran AmpliconSuite version 0.931.4 (https://github.com/AmpliconSuite/AmpliconSuite-pipeline) which invoked CNVkit (Talevich et al., 2016) to call genome-wide copy number (CN) profiles and identify seed amplicon intervals with CN values larger than 4.5 from these aligned WGS samples. We then ran AmpliconArchitect (AA) (Deshpande et al., 2019) version 1.3_r1 to infer the structure of focal amplifications from each sample, with the aligned WGS reads and seed amplicon intervals as input. A focal amplification is composed of a collection of genomic segments connected by breakpoints indicating either a CN change between two consecutive segments, or a rearrangement connecting two nonadjacent segments. A single sample can contain multiple non-overlapping focal amplifications. AA represents focal amplifications in the form of a copy-number aware breakpoint graph, where nodes represent genome segments and edges represent junctions between segments, including breakpoint connections. AA further decomposes the breakpoint graph into a collection of cyclic and non-cyclic paths, each representing a potential structure or substructure (i..e, local assembly) comprised of genome segments connected by a chain of breakpoints. The structural signatures in these paths are subsequently used to classify the type of focal amplification. Note that AA was run with parameters -insert_sdevs 9 to filter artifactual discordant reads and improve runtime performance, and default parameters otherwise.

Amplicon classification
We ran AmpliconClassifier version 0.4.10 (https://github.com/AmpliconSuite/AmpliconClassifier) using the AA-derived breakpoint graph and cycles files to classify each focal amplification into five categories: (1) cyclic amplification (potential ecDNAs); (2) BFB amplification; (3) Complex non cyclic amplification; (4) Linear amplification; and (5) Invalid focal amplification. We summarize the AmpliconClassifer rules (originally described in Kim et al. and Luebeck et al. (Kim et al., 2020; Luebeck et al., 2023)) as follows. As a prerequisite, focal amplifications must contain ≥10 kb of total genomic segments amplified to at least 5 copies above median ploidy to be considered valid. Focal amplifications were classified as BFB if they met the criteria for a BFB amplification (i.e., if breakpoints representing foldback events account for at least 25% of all SVs in the amplicon, and the cycles containing a foldback account for at least 60% of the length-weighted total CN of valid amplicon paths decomposed by AA). Focal amplifications not classified as BFB were classified as cyclic if there exists a cycle in the breakpoint graph (representing a potential ecDNA structure), and the total copy counts from cycles account for at least 12% of the total length-weighted CN. Acyclic focal amplifications were classified as complex non cyclic if they contained at least 5 breakpoint edges representing rearrangements, suggesting higher-order rearrangements beyond simple indel SV events. All other valid acyclic focal amplifications were classified as linear. We then hierarchically classified samples based on which type of focal amplifications were present in the sample, giving precedence to cyclic, followed by BFB, complex and linear. For example, a sample with both cyclic and complex focal amplifications would be classified as cyclic. Samples without any valid focal amplifications were similarly classified as 'no focal somatic CN amplification detected'.

HiChIP visualization at structural rearrangements with NeoLoopFinder

We ran NeoLoopFinder (Wang et al., 2021) version 0.2.5 to search for chromatin loops on rearranged genomes (corresponding to local assemblies of linked breakpoints) and CN-corrected H3K27ac HiChIP matrices. NeoLoopFinder, by default, computes a genome-wide CN profile and a collection of CN segments from an input HiChIP matrix, and then balances the matrix with a modified ICE procedure by taking the CN segments as input. Input cool files were generated at 10kb resolution from .hic files using HiCExplorer's hicConvertFormat (version 2.2) and balanced using cooler balance (version 0.9.1). We provided the NeoLoopFinder pipeline with CN segments estimated from the corresponding WGS samples (based on ASCAT CNV calls) as its input of the CN-aware matrix balancing procedure with NeoLoopFinder's correct-cnv. Given a list of candidate SVs (potentially from other sources, e.g., WGS or OM), NeoLoopFinder then reconstructs local assemblies representing a chain of one or more SVs from the input list, by shifting or flipping the submatrices according to the coordinates and orientations of the SVs. Therefore, we supplied NeoLoopFinder with a collection of SV breakpoints identified by BRASS from WGS data, which were filtered and used for complex SV assembly with NeoLoopFinder's assemble-complexSVs. In case NeoLoopFinder missed true assemblies, we additionally augmented the assemblies constructed by NeoLooFinder with the collection of local assemblies from AA cycle decomposition as follows. Because NeoLoopFinder does not accept assemblies with duplicated segments, we broke each cycle returned by AA into all possible longest paths of at least 2 non-overlapping segments. We provided these paths as input to NeoLoopFinder to search for chromatin loops in addition to the local assemblies constructed above using neoloop-caller -O neo-loops.txt allValidPairs.cool --assembly assemblies.txt --balance-type CNV --protocol insitu --prob 0.95 --nproc 20. The output of NeoLoopFinder consists of two types of interactions: 'loops,' which represent interactions on a single genomic segment, and 'neo-loops,' representing interactions on two different genomic segments, brought together by an SV. We postprocessed the loops and neoloops identified by NeoLoopFinder in each HiChIP sample (as case sample) by filtering out those that also occur in any other samples without focal amplifications on the same genomic segments (as control samples). In control samples, loops were searched on the same collection of local assemblies as used in the case sample. For comparing the number of loops per classification type, we dropped focal amplifications with total size less than 500kb, which often lead to unreliable classifications, as well as insufficient number of neighboring bins for loop finding.

Co-amplification frequency analysis across TCGA WGS
To identify potential enhancer regions co-focally-amplified with an oncogene of interest (for example, amplified on ecDNA), we binned each focally amplified genome with 10 kb resolution in accordance with HiChIP, and counted the number of samples co-amplified with the given oncogene per bin. Due to small cohort size (243 samples in total), the oncogene of interest is often amplified in very few samples. We overcome this limitation by counting, in each 10kb bin, the number of samples co-amplified with the given oncogene within a larger cohort of 1538 WGS samples from Kim et al (Kim et al., 2020). We computed an empirical P-value of co-amplification for each 10kb bin connected with the given oncogene by a loop or neoloop as follows: Let n0 be the number of samples where bin bi is co-amplified with gene g. To compute an empirical permutation based p-value, we generated 10,000 datasets randomly shuffling the focally amplified bins in each sample, such that (i) the distance between the first and last amplified bins after shuffling is at most that distance in the original amplification; (ii) the number of contiguously amplified intervals after shuffling remains the same as the number in the original amplification; and (iii) bins involving g are always amplified. The empirical p-value was given by the fraction of times bin bi was co-amplified with g in at least n0 samples. Finally, empirical P-values were adjusted for multiple comparisons using the Benjamini-Hochberg procedure.

Code Availability
Custom code used in this study is available at https://github.com/NCICCGPO/HiChIP-Manuscript.

For manuscripts utilizing custom algorithms or software that are central to the research but not yet described in published literature, software must be made available to editors and reviewers. We strongly encourage code deposition in a community repository (e.g. GitHub). See the Nature Portfolio guidelines for submitting code & software for further information.

Data

Policy information about availability of data

All manuscripts must include a data availability statement. This statement should provide the following information, where applicable:

- Accession codes, unique identifiers, or web links for publicly available datasets
- A description of any restrictions on data availability
- For clinical datasets or third party data, please ensure that the statement adheres to our policy

Processed data not provided in the supplementary data files is available through the TCGA Publication Page (https://gdc.cancer.gov/about-data/publications/TCGA-HiChIP-2024). Raw HiChIP data as fastq or aligned bam files are available through the NIH Genomic Data Commons portal (https://portal.gdc.cancer.gov/).
The processed RNA-seq, Genome-Wide SNP Array, DNA-methylation, and ATAC-seq data were downloaded from https://portal.gdc.cancer.gov/.
The processed scATAC-seq archR object (v1.0.1) with cell type annotation was downloaded from https://www.synapse.org/.
Cancer-associated SNP data were retrieved from the database available at https://www.ebi.ac.uk/gwas/. The LD data was sourced from the haploreg website (http://archive.broadinstitute.org/mammals/haploreg/data/).

Research involving human participants, their data, or biological material

Policy information about studies with human participants or human data. See also policy information about sex, gender (identity/presentation), and sexual orientation and race, ethnicity and racism.

Reporting on sex and gender	Included in Supplementary Table 1.
Reporting on race, ethnicity, or other socially relevant groupings	Included in Supplementary Table 1.
Population characteristics	Samples were selected from the set of samples previously profiled by bulk ATAC-seq to span the 16 cancer types profiled in this manuscript with a focus on breast cancer and at least 3 samples for each other cancer. Within breast cancer, 3 samples were selected from each major breast cancer subtype (Basal, HER2, LumA, LumB). Samples were prioritized for selection

	based on high data quality in previous bulk ATAC-seq experiments and the availability of sufficient nuclei in cryopreserved stocks. Other inclusion or exclusion criteria were not assessed. Additional characteristics including participant age are available at https://portal.gdc.cancer.gov/
Recruitment	All recruitment was done by The Cancer Genome Atlas.
Ethics oversight	This study complied with all relevant ethical regulations and ethical guidance was overseen by the TCGA Program Office. Each study site that contributed biological material had its own ethics board approval. TCGA ethics policies are available at https://www.cancer.gov/ccg/research/genome-sequencing/tcga/history/ethics-policies

Note that full information on the approval of the study protocol must also be provided in the manuscript.

Field-specific reporting

Please select the one below that is the best fit for your research. If you are not sure, read the appropriate sections before making your selection.

☒ Life sciences ☐ Behavioural & social sciences ☐ Ecological, evolutionary & environmental sciences

For a reference copy of the document with all sections, see nature.com/documents/nr-reporting-summary-flat.pdf

Life sciences study design

All studies must disclose on these points even when the disclosure is negative.

Sample size	Samples were selected from the set of samples previously profiled by bulk ATAC-seq to span the 16 cancer types profiled in this manuscript with a focus on breast cancer and at least 3 samples for each other cancer. Within breast cancer, 3 samples were selected from each major breast cancer subtype (Basal, HER2, LumA, LumB). Samples were prioritized for selection based on high data quality in previous bulk ATAC-seq experiments and the availability of sufficient nuclei in cryopreserved stocks. Other inclusion or exclusion criteria were not assessed.
Data exclusions	No data were excluded.
Replication	Replication was not performed due to limited availability of biological material and input requirements for HiChIP library generation.
Randomization	No randomization was done to allocate samples into experimental groups.
Blinding	The samples we analyzed were deidentified by The Cancer Genome Atlas. The investigators were not blinded to group allocation during experiments and outcome assessment.

Reporting for specific materials, systems and methods

We require information from authors about some types of materials, experimental systems and methods used in many studies. Here, indicate whether each material, system or method listed is relevant to your study. If you are not sure if a list item applies to your research, read the appropriate section before selecting a response.

Materials & experimental systems

n/a	Involved in the study
☐	☒ Antibodies
☒	☐ Eukaryotic cell lines
☒	☐ Palaeontology and archaeology
☒	☐ Animals and other organisms
☒	☐ Clinical data
☒	☐ Dual use research of concern
☒	☐ Plants

Methods

n/a	Involved in the study
☒	☐ ChIP-seq
☒	☐ Flow cytometry
☒	☐ MRI-based neuroimaging

Antibodies

Antibodies used	All HiChIP was performed using H3K27ac as the target (Abcam ab4729). 2 ug of H3K27ac antibody was used per sample with one million cells as input.
Validation	The antibodies are validated for use on human samples on the manufacturer's websites and give highly reproducible results with published positive control data-sets including ChIP-seq data from primary tissues and ATAC-seq from matched tumor samples.

Plants

Seed stocks	*Report on the source of all seed stocks or other plant material used. If applicable, state the seed stock centre and catalogue number. If plant specimens were collected from the field, describe the collection location, date and sampling procedures.*
Novel plant genotypes	*Describe the methods by which all novel plant genotypes were produced. This includes those generated by transgenic approaches, gene editing, chemical/radiation-based mutagenesis and hybridization. For transgenic lines, describe the transformation method, the number of independent lines analyzed and the generation upon which experiments were performed. For gene-edited lines, describe the editor used, the endogenous sequence targeted for editing, the targeting guide RNA sequence (if applicable) and how the editor was applied.*
Authentication	*Describe any authentication procedures for each seed stock used or novel genotype generated. Describe any experiments used to assess the effect of a mutation and, where applicable, how potential secondary effects (e.g. second site T-DNA insertions, mosiacism, off-target gene editing) were examined.*